JGR Space Physics

RESEARCH ARTICLE
10.1029/2023JA032078

Quiet Time Thermospheric Gravity Waves Observed by GOCE and CHAMP

Shuang Xu[1], **Sharon L. Vadas**[2], **and Jia Yue**[3,4]

[1]Department of Atmospheric and Planetary Sciences, Hampton University, Hampton, VA, USA, [2]Northwest Research Associates, Boulder, CO, USA, [3]Physics Department, Catholic University of America, Washington, DC, USA, [4]Catholic University of America/NASA Goddard Space Flight Center, Greenbelt, MD, USA

Key Points:

- The strongest gravity wave (GW) events occur most often in the summer polar region during geomagnetic quiet times
- GWs in the winter hemisphere at midlatitudes during quiet times and 12–24 local solar time (LST) are possible due to the polar vortex
- CHAllenging Minisatellite Payload observes a clockwise (counterclockwise) rotation of GW azimuth in the northern (southern) hemisphere over LST

Correspondence to:

S. Xu,
xushuang9999@gmail.com

Citation:

Xu, S., Vadas, S. L., & Yue, J. (2024). Quiet time thermospheric gravity waves observed by GOCE and CHAMP. *Journal of Geophysical Research: Space Physics*, *129*, e2023JA032078. https://doi.org/10.1029/2023JA032078

Received 12 SEP 2023
Accepted 10 DEC 2023

Author Contributions:

Conceptualization: Shuang Xu, Sharon L. Vadas
Data curation: Shuang Xu
Formal analysis: Shuang Xu, Sharon L. Vadas
Funding acquisition: Sharon L. Vadas, Jia Yue
Investigation: Shuang Xu, Sharon L. Vadas, Jia Yue
Methodology: Shuang Xu, Sharon L. Vadas, Jia Yue
Project Administration: Sharon L. Vadas, Jia Yue
Resources: Shuang Xu, Sharon L. Vadas
Software: Shuang Xu
Supervision: Sharon L. Vadas, Jia Yue
Validation: Shuang Xu
Visualization: Shuang Xu
Writing – original draft: Shuang Xu

Abstract The Gravity Field and Steady-State Ocean Circulation Explorer (GOCE) and CHAllenging Minisatellite Payload (CHAMP) satellites measure in-situ thermospheric density and cross-track wind. When propagating obliquely to the satellite track in a horizontal plane (i.e., not purely along-track or cross-track), gravity waves (GWs) can be observed both in the density and cross-track wind perturbations. We employ the Wavelet Analysis, red noise model, dissipative dispersion and polarization relations for thermospheric GWs, and specific criteria to determine whether a quiet-time (Kp < 3) thermospheric traveling atmospheric disturbances (TADs) event is a GW or not. The first global morphology of thermospheric GWs instead of TADs is reported. The fast intrinsic horizontal phase speed (c_{IH} > 600 m/s) of most GWs suggests that they are not generated in the lower/middle atmosphere (where c_{IH} < 300 m/s). A second population of GWs with slower speeds (c_{IH} = 50–250 m/s) in GOCE are likely from the lower/middle atmosphere, but they occur much less frequently in CHAMP. GW hotspots occur during the high-latitude and the winter midlatitude regions. GW amplitudes exhibit semi-annual and annual variations. These findings suggest that most GOCE and CHAMP GWs are higher-order GWs from primary GW sources in the lower/middle atmosphere. Finally, the average propagation direction of the CHAMP GWs exhibits a clear diurnal cycle, with clockwise (counterclockwise) occurring in the northern (southern) hemisphere and equatorward propagation occurring at ~13 LST. This suggests that the predominant GW propagation direction is opposite to the background wind direction.

Plain Language Summary Gravity waves (GWs) are challenging to measure in many parts of the thermosphere. Still, the GOCE and CHAMP missions offer an opportunity to observe GWs by measuring thermospheric density and cross-track wind perturbations. However, the absence of along-track wind perturbations in these data sets hinders the direct determination of intrinsic GW parameters. To address this, we employ Wavelet Analysis and red noise processes to quantify the along-track parameters, including phases and amplitudes, of intermittent and localized thermospheric traveling atmospheric disturbance (TAD) events of varying scales. Subsequently, we utilize the transformed dissipative dispersion and polarization relations for thermospheric GWs to determine intrinsic parameters of GWs in those TAD events. By examining the resulting GW solutions (e.g., propagation directions, horizontal wavelengths, periods, etc.), we investigate the characteristics of thermospheric GWs during geomagnetic quiet time. We present first statistics on global thermospheric GW properties across different latitudes, local times, and months. The high phase speeds of most GWs suggest that they cannot be directly generated in the lower/middle atmosphere. Our findings reveal an evident seasonal variation of GW amplitudes, and their diurnal cycle in predominant propagation directions are opposite to the background wind direction.

1. Introduction

Atmospheric gravity waves (GWs) play a fundamental role in the redistribution of energy and momentum throughout Earth's atmosphere, influencing its dynamics across various spatial and temporal scales. The sources of GWs encompass a range of atmospheric phenomena, and include orographic effects induced by wind flow over mountains (M. J. Alexander & Teitelbaum, 2007, 2011; Becker & Vadas, 2020; Eckermann & Preusse, 1999; Fritts et al., 2016; Hindley et al., 2021; L. Hoffmann et al., 2013; Lund et al., 2020; Plougonven et al., 2008; Preusse et al., 2002; Sato et al., 2012; Vadas & Becker, 2019), convective processes in the atmosphere (M. J. Alexander et al., 1995; Choi et al., 2007; Fovell et al., 1992; Heale et al., 2019; Holt et al., 2017; Holton & Alexander, 1999; Horinouchi et al., 2002; Lane et al., 2001; Lane et al., 2003; H. L. Liu et al., 2014; Piani et al., 2000; Song et al., 2003; Stephan & Alexander, 2015; Taylor & Hapgood, 1988; Yue et al., 2009), adjustments within

Writing – review & editing: Shuang Xu, Sharon L. Vadas, Jia Yue

jet streams and frontal systems (Fritts & Luo, 1992; Watanabe et al., 2008; Wu & Zhang, 2004; Zhang, 2004), wind shear-induced imbalances (Fritts, 1982), wave-wave interactions (Wüst & Bittner, 2006), higher-order wave excitation from wave dissipation (Becker & Vadas, 2020; Becker, Vadas, et al., 2022; Vadas & Becker, 2019; Vadas, Becker, Bossert, et al., 2023; Vadas, Becker, Figueiredo, et al., 2023; Vadas, Figueiredo, et al., 2023; Vadas et al., 2003, 2018), Joule heating during geomagnetic storms (Barth, 2010; Hocke & Schlegel, 1996; Richmond, 1978), the spontaneous emission from the polar vortex (Becker, Vadas, et al., 2022; O'sullivan & Dunkerton, 1995; Vadas, Becker, Bossert, et al., 2023; Yoshiki & Sato, 2000), as well as rare events like tsunamis (Azeem et al., 2017; R. F. Garcia et al., 2014; Vadas et al., 2015) and volcanic eruptions (Vadas, Becker, Figueiredo, et al., 2023; Wright et al., 2022; Yue et al., 2022). Understanding the dynamics related to GWs is important not only for Earth's atmosphere but also for other planetary atmospheres (e.g., Sánchez-Lavega et al., 2017), including exoplanets.

The influence of GWs becomes pronounced in the middle and upper atmosphere, impacting the variability, winds and temperatures, and global circulation. It is well known that GWs serve as drivers for global-scale phenomena such as the quasi-biennial oscillation (Baldwin et al., 2001) and the mesospheric residual circulation (Holton, 1982). Recently, there has been a growing interest in understanding the connection between lower and middle atmospheric activities, such as the effects that GWs from the polar vortices have on the variability of the thermosphere and ionosphere. For instance, studies have revealed that during periods of weakened polar vortex states, the upper stratosphere and lower mesosphere experience reduced GW activities (Harvey et al., 2023), resulting in weaker thermospheric GW activities (Becker, Vadas, et al., 2022) and fewer traveling ionospheric disturbances (TIDs) (Frissell et al., 2016). These findings underscore the intricate interplay between lower atmospheric dynamics and the behavior of GWs throughout the atmosphere, offering insights into the broader impacts of atmospheric processes from below.

GWs are also important to telecommunication and satellite operation. Perturbations in the thermosphere (e.g., the occurrence of equatorial spread *F*, also called equatorial plasma bubbles) have received intensive attention because of their complex physics and severe influence on telecommunication and navigation (Aa et al., 2020). The seeding of those phenomena is the least understood, and GWs have been commonly suggested to play a key role in the seeding process (H. X. Liu et al., 2017; Takahashi et al., 2009).

Although thermospheric GWs play a vital role in thermospheric dynamics, their measurement in this region is challenging. Previous studies have employed indirect methods to study thermospheric GWs. For example, Bhatt et al. (2023) utilized airglow perturbations captured by optical sensors like all-sky imagers and Fabry-Perot Interferometers to derive nighttime wind and temperature perturbations. Another approach uses Global Positioning System (GPS) Total Electron Content data sets to retrieve GW characteristics from TIDs around the F2 layer (Azeem et al., 2015; Nishioka et al., 2013; Xu et al., 2019). These data have high horizontal and temporal resolution, but are limited to regions with dense ground-based receiver networks, such as the continental US. Satellite-based remote sensing methods have also provided valuable observations in the thermosphere/ionosphere; however, they are subject to limitations of low time or horizontal resolution. For instance, the TIMED Doppler Interferometer (TIDI) onboard the Thermosphere, Ionosphere, Mesosphere Energetics and Dynamics (TIMED) satellite and Michelson Interferometer for Global High-resolution Thermospheric Imaging (MIGHTI) onboard Ionospheric Connection Explorer (ICON) satellite measure horizontal wind profiles along the satellite orbit but with coarse horizontal resolution (~750 km for TIDI (Yee et al., 2003) and 250–500 km for MIGHTI (Cullens et al., 2022; Dhadly et al., 2021)); The Global-scale Observations of the Limb and Disk (GOLD) mission can observe neutral temperature disturbances at an altitude of ~150 km, but with coarse horizontal (250×250 km^2 at nadir) and time resolutions (~30-min cadence for day disk images) (McClintock et al., 2020). To overcome these limitations, in-situ spacecraft missions equipped with precise accelerometers have emerged as powerful tools for studying traveling atmospheric disturbances (TADs) and thermospheric GWs. Low Earth orbit (LEO) missions such as CHAMP, GOCE, and Gravity Recovery and Climate Experiment (GRACE) have provided unprecedented accuracy and resolution in density and cross-track wind measurements (Doornbos, 2012). Previous studies have detected TADs, which include GWs, using accelerometer data onboard several spacecrafts (e.g., Bruinsma & Forbes, 2008; Li et al., 2023; H. Liu et al., 2017; Park et al., 2014, 2023; Trinh et al., 2018). However, due to the absence of along-track wind measurements, these studies have primarily focused on either density or cross-track wind disturbances along the satellite track. Whether these TADs are GWs or not is not known without detailed investigation of each event.

Vadas et al. (2019) carried out a case study by extracting the intrinsic characteristics (including the propagation direction) of hotspot GWs from a single track of observations as GOCE passed over the Southern Andes using the formalism presented in Vadas and Nicolls (2012). That study found that most of the extracted GWs had such fast phase speeds that they must have been generated in the thermosphere. However, the methodology in that work was rudimentary and difficult to apply for a GW climatology study over a long period. Xu et al. (2021) analyzed the thermospheric density data provided by GOCE (June–August 2010–2013) and CHAMP (June–August 2004–2007) to study high latitude TADs in the austral winter. They extracted the TADs along the satellite tracks from density for varying Kp indices, and linearly extrapolated the TAD distribution to $Kp = 0$. For the first time, they found that TADs near the south pole during geomagnetic quiet times were mainly higher-order GWs "from below" (i.e., the primary GWs were from the lower/middle atmosphere, such as orographic forcing over the Southern Andes Mountains). Whereas during geomagnetic storms with K$p > 4$, the TADs were mainly excited by auroral heating around the aurora oval. Although GOCE and CHAMP data sets provide high-quality observations of TADs, the TADs studied in Xu et al. (2021) were a function of the along-track horizontal wavelength λ_{track} instead of the horizontal wavelength along the GW propagation direction λ_H.

Building upon the high-quality observations from the GOCE and CHAMP, this paper aims to overcome the challenge posed by the absence of along-track wind perturbations and unravel the intrinsic characteristics of the thermospheric GW events observed by these satellites as along-track TADs. In this novel approach, we analyze the wave packets associated with each TAD event to determine if they exhibit the characteristic propagation behavior of thermospheric GWs. We utilize the dissipative polarization and dispersion relationship of GWs from Vadas and Fritts (2005), along with background atmospheric conditions, to derive a more comprehensive understanding of the intrinsic properties of GWs, including their propagation directions, intrinsic period (τ_I), horizontal wavelength (λ_H), and more. We also apply this method to the GOCE GWs generated by the Tohoku earthquake/tsunami in 2011 (Appendix F). This innovative method holds the potential for studying thermospheric GWs observed by other LEO satellite missions that provide similar data sets derived from *in-situ* measurements (e.g., measurements via accelerometer instruments such as GRACE/GRACE Follow-On (GRACE-FO) (Siemes et al., 2023; Tapley et al., 2004) and the Swarm constellations (Olsen et al., 2013)), or via mass spectrometer instruments such as Geospace Dynamics Constellation (GDC) (Benna et al., 2022). This broadens the prospects for the application of our methodology in the investigation of GWs across different satellite missions, enhancing our understanding of thermospheric GWs at different altitudes.

The paper is arranged as follows: In Section 2, we describe the GOCE and CHAMP data sets. In Section 3, we introduce (a) the methodology to pick out TADs through rectified Wavelet analysis and (b) the methodology to determine the GW intrinsic parameters (λ_H, λ_z, c_H, τ_{Ir} and their direction of propagation) using the dissipative GW dispersion and polarization relations, and to verify those TADs that are GWs by these solved intrinsic parameters. In Section 4, we show statistical (seasonal/monthly) results of thermospheric GWs obtained from GOCE and CHAMP data sets. Section 5 provides conclusions and an outlook.

2. GOCE and CHAMP Data Sets

The GOCE satellite was a European Space Agency mission that aimed to improve our understanding of Earth's gravity field and geodynamics. Launched on 17 March 2009, GOCE orbited Earth at an unusually low altitude of ∼250–290 km with an inclination of ∼96.7°, and local solar time (LST) of its ascending node drifted slowly from 18:13 LST (2009 November) to 19:33 LST (2013 October) (Doornbos, 2019). To maintain its low altitude for four to 5 years, the satellite used an ion thruster assembly that aligned with the orbit direction. GOCE carried a payload Electrostatic Gravity Gradiometer that consisted of six highly accurate accelerometers with a noise level of 10^{-12} m s^{-2} Hz$^{-1/2}$ (Doornbos et al., 2009; Visser et al., 2018). The orbital period of GOCE was ∼90 min.

The CHAMP mission was led by the GeoForschungsZentrum (GFZ, or Geo-research Centre) and launched on 15 July 2000, with the primary objective of measuring Earth's gravity and magnetic field to high precision. CHAMP was in a near-circular orbit with an inclination of ∼87°, and its ascending and descending nodes covered all LST (24-hr) about every four months. The satellite's altitude decreased gradually from 450 km at the beginning of the mission to 260 km in August 2010. The orbital period of CHAMP was about ∼90 min, with a slight decrease of ∼5 min due to its descending altitude during its life span. Equipped with a Spatial Triaxial Accelerometer for Research (STAR) accelerometer, the measurements of CHAMP were less precise than those of GOCE. The STAR accelerometer had a sensor in the axis parallel to the Z-axis of the satellite body-fixed

frame (nominally pointed toward the satellite's nadir) that suffered from a malfunction, and was less sensitive than the sensors along the other two axes, but STAR still had a resolution $<3 \times 10^{-9}$ m s^{-2} Hz$^{-1/2}$ (Rodrigues et al., 2003), which was adequate for deriving in-situ density and cross-track wind measurements and TAD analysis. For both GOCE and CHAMP, we specifically select TAD and GW events that occurred when both concurrent Kp and the average Kp over the past 6 hr were less than 3, aiming to minimize wave events excited by geomagnetic disturbances.

Doornbos et al. (2010) described the methodology for deriving in-situ density and cross-track wind measurements for the CHAMP mission. The approach for retrieving the density and cross-track wind for GOCE were essentially identical (Doornbos et al., 2013). First, when initially assuming a co-rotating thermosphere with density but no wind suggested by the Mass Spectrometer and Incoherent Scatter radar (MSIS) model, the modeled acceleration experienced by a spacecraft does not align with the measured acceleration. The discrepancy between the measured and modeled accelerations is mainly due to two parts: the directional discrepancy is attributed to the absence of cross-track wind in the model, the magnitude discrepancy is attributed to incorrect model density. To address this, a cross-track wind is introduced to the relative velocity (the difference between the bulk velocity of gas particles and the spacecraft velocity), and the absolute in-situ mass density is adjusted at each iterative step. This gradual iteration allows the modeled acceleration to converge toward the observed aerodynamic accelerations. It should be noted that the in-track wind is assumed according to a model value (Doornbos, 2019). However, given that the magnitude of in-track wind ($\sim$ a few hundreds of m/s at most) is significantly smaller than the spacecraft velocity ($\sim$8 km/s), and the low frontal area-to-mass ratio of the spacecraft, it was impossible to distinguish how much in total in-track acceleration discrepancy was induced by the in-track wind deviation and density deviation (Doornbos, 2012; Doornbos et al., 2010). In principle, the wind component in the vertical direction could be derived in a similar way as the cross-track wind, but there are two obstacles to overcome for CHAMP: (a) aerodynamic acceleration in the vertical direction is in general too small when compared with errors in the instrument calibration, the radiation pressure model, and the lift force model; (b) the malfunction of the CHAMP accelerometer in *Z*-axis prevents the acquisition of data in the vertical direction (Doornbos et al., 2010). Therefore, only the density perturbation and cross-track wind are available in the CHAMP data set analyzed in this paper. Because the GOCE mission carried more advanced accelerometers than CHAMP, its measurements have the capacity to derive both cross-track and vertical winds, for example, R. F. Garcia et al. (2014) introduced disturbances in both cross-track and vertical winds from the Tohoku earthquake and tsunami occurred in 2011. However, in the public-released the GOCE data set, the vertical component of the crosswind is assumed to be zero (Doornbos, 2019), the vertical wind perturbations are thus not publicly available in the GOCE and CHAMP data sets; instead, the density and cross-track wind data sets are available and are used in our study.

In this study, our primary focus lies on the density and cross-track wind observations obtained from GOCE during November 2009 to October 2013 and from CHAMP during 2004–2007, when satellites were at relatively stable altitudes ($\sim$270 km for GOCE and $\sim$370 km for CHAMP). The data were sampled at a rate of 1 data point every 10 s (or 80 km in distance) for both GOCE and CHAMP, with the *Kp* index provided every 3 hr. Based on Doornbos et al. (2010), the rms density and wind errors in the data can be as low as 0.03% and 1 m/s, respectively. Although the systematic density error in CHAMP was estimated to be around $\sim$10%–15%, the same algorithm applied to GOCE data could potentially yield even smaller rms errors due to the presence of more and better instruments onboard. These favorable error characteristics allow us to study relatively small-amplitude and small-scale perturbations such as TADs and GWs. To provide accurate estimates of the errors associated with each observed wave event, we developed specific techniques, described in Section 3 of this paper.

3. Techniques for Diagnosing GWs From *In-Situ* Observations

The *in-situ* GOCE and CHAMP measurements provide valuable information about the amplitudes and scales of TADs along the satellite tracks. However, due to the presence of intrinsic noise in these measurements, it can be difficult to distinguish between noise and meaningful physical variations in the thermosphere. Despite this challenge, previous studies have successfully employed statistical methods to accurately represent the seasonal and global distribution of TADs from GOCE and CHAMP measurements (e.g., Forbes et al., 2016; H. X. Liu et al., 2017; Park et al., 2014; Trinh et al., 2018; Xu et al., 2021). In this study, we present a novel method to identify TADs from noise (Section 3.1) and then solve GWs from the TADs (Section 3.2).

3.1. Diagnosing TADs Using Rectified Wavelet Analysis Method and Red-Noise Model

Wavelet analysis is chosen as the preferred method in our study due to its ability to effectively handle localized and non-stationary wave packets, which are common in real-world scenarios. While the Fast Fourier transform (FFT) is suitable for quantifying perturbations with fixed wavelengths across short satellite tracks (e.g., Vadas et al., 2019), it may not work when wave packets have varying scales, frequencies, and phases, and when multiple wave packets are superimposed, making their separation challenging. In contrast, wavelet analysis offers a powerful approach to separate each wave packet based on its dominant period, amplitude, location, and duration. Wavelet analysis has been widely utilized by researchers, including Torrence and Compo (1998, hereafter TC98) and Chen (2016, hereafter C16). The versatility and effectiveness of wavelet analysis make it suitable for investigating the complex wave packets here.

The wavelet analysis derives a spectrum of variations arising from both noise and variations of TADs. To differentiate between perturbations with low confidence (noise) and high confidence (TADs), we assume that the noise can be modeled by red noise. The red noise model assumes that noise has a power (variance) spectral density that decreases as the scale decreases whereas the white noise model assumes that noise with different scales have equal power. In line with TC98, we first calculate the autocorrelation of the input series, which can be used to derive the expected normalized power of noise at each frequency. In this way, we can estimate the errors even though quantitative uncertainties for each data point are unavailable. Many geophysical time series can be modeled as either white noise or red noise (TC98). For instance, TC98 modeled the noises in the Niño3 sea surface temperature time series using the red-noise model. They then established significance levels and confidence intervals to diagnose wave packets with higher than 95% confidence level.

The univariate lag-1 autoregressive red noise model proposed by TC98 is a valuable technique for processing a large number of TADs, especially in scenarios where the input series is primarily governed by stochastic noise with different scales. Due to its effectiveness and computational efficiency under such assumptions, it serves as a practical and cost-effective method for automated processing. However, it is essential to recognize that the red noise model may not be suitable for all situations. In cases where the input series exhibits variations dominated by different scales of signals rather than noise, the red noise technique can lead to underestimating the confidence for TADs. Consequently, this may result in an underestimation of the number of TADs identified in the data set. Improving the estimation of confidence in each wave/noise packet remains a challenge. To address this limitation and achieve more accurate results, further investigations into the noise characteristics of the GOCE and CHAMP data sets are required. This additional effort will be critical for enhancing the robustness of our findings and ensuring the reliability of the outcomes obtained through the red noise model.

By following the practical guide provided in TC98, we calculate the wavelet power spectra $|W(n, \lambda_{\text{track}})|^2$ for density and cross-track wind as functions of the data point index (n) and the along-track wavelength (λ_{track}, which takes into account the satellite motion, see Appendix D for more details). These power spectra quantify the TADs along the satellite track. However, the TC98 method is biased toward larger scales when the input is considered as a superposition of monochromatic waves (Y. Liu et al., 2007; Maraun & Kurths, 2004). To reduce this bias, C16 replaced the wavelet function $\hat{\psi}(s\omega_k)$ in TC98 with a modified wavelet function $\hat{\psi}_{\text{mod}} = C_F\hat{\psi}$. We adopted this change to obtain an unbiased wavelet spectrum $W_{\text{mod}} = 2C_F W$ which we use to quantify the amplitudes and phases of TAD events in density and cross-track wind. Here, the correction factor C_F is a function of λ_{track}, and is defined in Appendix B.

In processing the GOCE and CHAMP data, it is common to encounter gaps in the measurements due to missing data. To address this issue and other computational considerations, we have divided the GOCE and CHAMP data sets into segments that are typically one full-circle orbit long. In Figure 1, we present the procedure for determining TADs in the density and cross-track wind data using a full-circle GOCE orbit on 5 July 2010 at 22:10–23:40 as an example. The full-circle GOCE orbit (red dots) begins in the westward direction (open red circle) and ends at the solid red circle (in the Northern Hemisphere). This orbit starts with the GOCE satellite in a descending mode and ends after completing the following ascending mode, which we refer to as the "DA (Descending-Ascending) mode." Due to the flattening of the reference ellipsoid representing the oblate Earth, the eccentricity of the orbit, and the perigee rotation rate, the altitudes of GOCE varies periodically (Doornbos et al., 2013). Figure 1b shows the in-situ density observation versus altitude within the track. From the relationship between the log-scaled density and height, we derive the thermospheric density scale height. To eliminate the density variation caused by the altitude change, we extrapolate the measured density

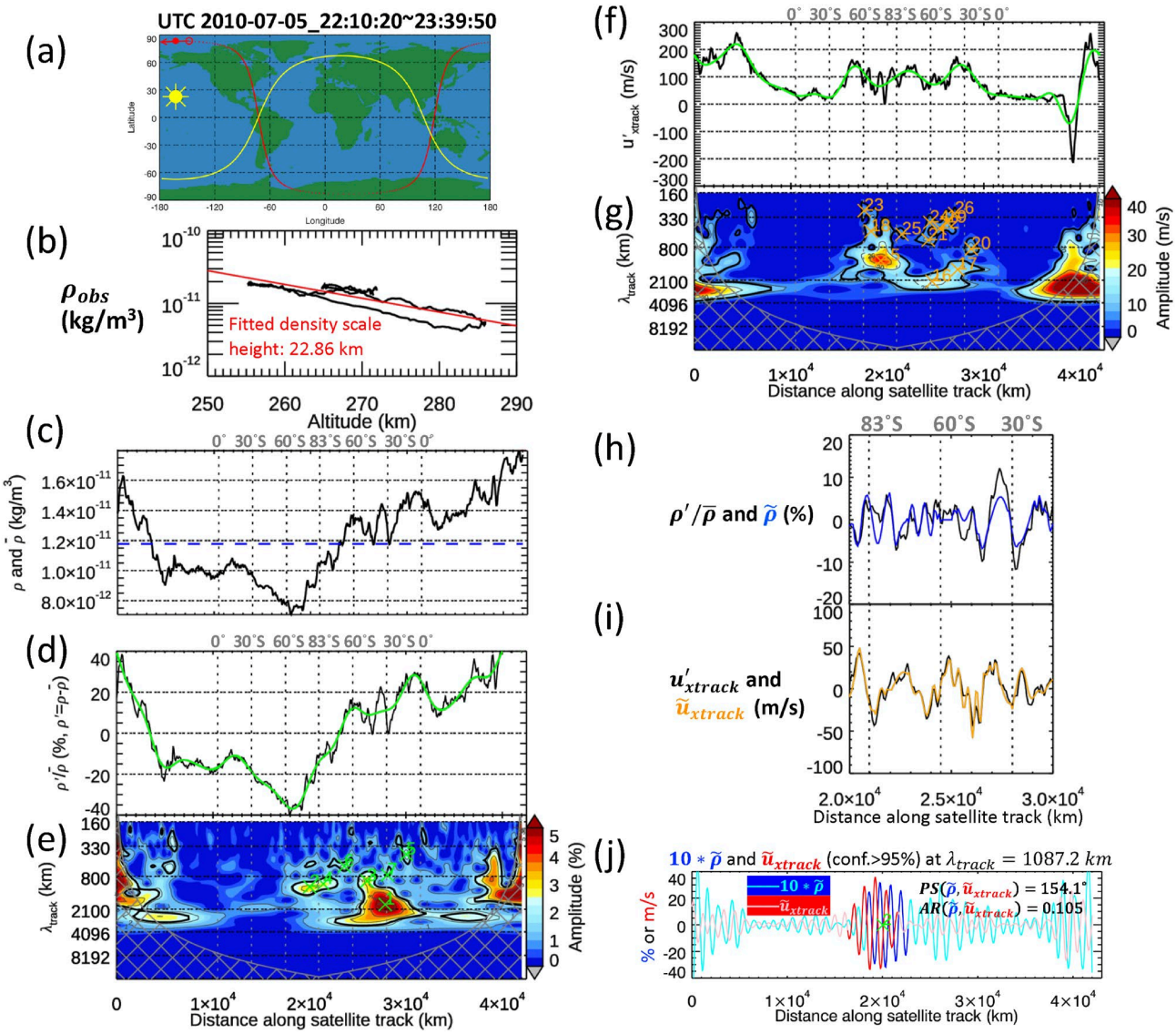

Figure 1. The procedure to identify a traveling atmospheric disturbance (TAD) event from GOCE density perturbations and cross-track wind. (a) The positions of GOCE data points over one full circle track divided by "DA mode" during Coordinated Universal Time (UTC) 2010-07-05_22:10:20~23:39:50 (red dots), subsolar point (yellow sun symbol) and day-night terminator (yellow curve). The red westward arrow denotes the satellite direction when GOCE starts this track. The open/filled red circle denotes the first/last position of the data point in this track. (b) GOCE in-situ measured density ρ_{obs} in log scale versus altitude within this orbit (black). The density scale height is derived from the slope of the linear-fitted line (red) of the log-scaled densities. (c) The black curve presents density (ρ) that are extrapolated to z = 270 km according to the measured thermospheric density scale height as a function of distance along the satellite track. The blue dashed line denotes the mean extrapolated density in this orbit at z = 270 km ($\bar{\rho}$). (d) Relative density perturbation in percent, $\rho'/\bar{\rho}$ (black, where $\rho' = \rho - \bar{\rho}$). The green curve denotes the background density for wavelengths ≥3,000 km. (e) Unbiased amplitude spectrum of the detrended (λ_{track} < 3,000 km) relative density perturbation ($\rho'/\bar{\rho}$). The thick black contour encloses TADs with >95% confidence for a red-noise process. Within the >95% confidence contours, peaks labeled with green crosses and green indices denote locations of TADs in density. Gray cross-hatched regions indicate the "cone of influence," where edge effects are important and waves are not trustworthy. (f–g) The same as (d–e) but for cross track wind perturbation u'_{xtrack}. In panel (g), peaks labeled with orange crosses and orange indices denote locations of TADs in cross-track wind. (h) Comparison between the sum of reconstructed perturbations $\tilde{\rho}$ (blue, λ_{track} < 3,000 km, confidence>95%) and the original detrended $\rho'/\bar{\rho}$ (black, λ_{track} < 3,000 km). The horizontal axis only spans from 2 × 10^4 to 3 × 10^4 km. (i) The same as (g) but for reconstructed perturbations $\tilde{u}_{xtrack}$ (orange, λ_{track} < 3,000 km, confidence>95%) and detrended u'_{xtrack} (black, λ_{track} < 3,000 km). (j) The reconstructed perturbation pair of 10 ∗ $\tilde{\rho}$ (dark and light blue) and $\tilde{u}_{xtrack}$ (dark and light red) at λ_{track} = 1,087.2 km. The dark/light color denotes perturbations with confidence higher/lower than 95%. The "PS" means "phase shift" in units of degrees, "AR" means "amplitude ratio" in units of %*s/m.

to a fixed altitude, which is 270 km for GOCE and 370 km for CHAMP, based on the thermospheric density scale height in the observation. As shown in Figure 1c, the extrapolated density is denoted as ρ, which is the sum of the background density $\bar{\rho}$ (defined by the average of the density at the extrapolated altitude) plus the

perturbation density ρ'. Figure 1d shows the relative density perturbation (black), defined as $\rho'/\overline{\rho}$. Figure 1e shows the unbiased wavelet spectrum $|W_{\text{mod}}|$ in $\rho'/\overline{\rho}$ for TADs with $\lambda_{\text{track}} < 3{,}000$ km in the relative density perturbation. The cross-hatched region shows the so-called "cone of influence" where edge effects are important. We only analyze TADs inside the center half of the orbit and outside of the "cone of influence". In the DA mode, TADs in the Southern Hemisphere are free from the edge effects on either end of the track, allowing us to focus on the peaks within the middle part of this circular orbit. To study TADs in the Northern Hemisphere, we re-process the same data set but divide the orbits by the "AD (Ascending-Descending) mode", so the "cone of influence" (endpoints) will be in the Southern Hemisphere. If a peak is located inside the thick black contours in Figure 1e, we have confidence higher than 95% that this peak is caused by a TAD rather than noise (Appendix B contains further information about the "confidence level of 95%".). For TADs in the cross-track wind, we directly extract the TADs from the observations since the wind is much less sensitive to changes in the altitude than the density. Figure 1f shows the cross-track wind perturbation (black), defined as u'_{xtrack}. Figure 1g shows the unbiased wavelet spectrum $|W_{\text{mod}}|$ in u'_{xtrack} with scales $\lambda_{\text{track}} < 3{,}000$ km. By analyzing the amplitude $|W_{\text{mod}}|$ (as shown in Figures 1e and 1g), and $\arg(W_{\text{mod}})$ (not shown), it is possible to reconstruct waves at different scales of λ_{track}. Each peak in Figures 1e and 1g that is not in the cone of influence and has a confidence level higher than 95% represents a likely TAD event. The position of a TAD event along the track and λ_{track} are determined from the horizontal and vertical coordinates of the peak. In Figures 1h and 1i, the sum of the reconstructed small-scale perturbations for TADs with $\lambda_{\text{track}} < 3{,}000$ km and confidence>95% (blue for relative density perturbation $\tilde{\rho}$, orange for $\tilde{u}_{\text{xtrack}}$) is compared to the original observed perturbation (black curves). By $\tilde{\rho}$ and $\tilde{u}_{\text{xtrack}}$ we mean $\rho'/\overline{\rho}$ and u'_{xtrack} for the reconstructed TADs, respectively. The reconstructed sum represents the principal components of the identified TADs after removed the noise via the red-noise model.

In Figure 1j, the component of one TAD (having $\lambda_{\text{track}} = 1{,}087.2$ km) is shown; the value of λ_{track} is the y-axis of TAD wave packet #2 in Figure 1e. The phase shift (PS) between $\tilde{\rho}$ and $\tilde{u}_{\text{xtrack}}$ ($PS(\tilde{\rho}, \tilde{u}_{\text{xtrack}})$) for this TAD is 154.3°, meaning that $\tilde{\rho}$ leads $\tilde{u}_{\text{xtrack}}$ by 154.3° along the satellite track inside the high confidence region. Simultaneously, the amplitude ratio (AR) between $\tilde{\rho}$ and $\tilde{u}_{\text{xtrack}}$ ($AR(\tilde{\rho}, \tilde{u}_{\text{xtrack}})$) is 0.105. However, quantifying the confidence of a TAD is not enough. According to the red-noise model, uncertainties in $\tilde{\rho}$ and $\tilde{u}_{\text{xtrack}}$ at a specific scale of λ_{track} can be estimated because $W_{\text{mod}}(n,\lambda_{\text{track}})$ is predicted to be a 2D normal distribution (see Equations (B9) and (B12)). For each TAD event in our program, we apply a Monte Carlo simulation to generate an N-element complex array ($N = 1{,}000$ in current study) so that the N-element phasor array of $\tilde{\rho}$ satisfies the 2D normal distribution in complex plane (a phasor is a complex number that represents a sinusoidal function.) The same process is applied to the phasor of $\tilde{u}_{\text{xtrack}}$ to generate an independent stochastic N-element complex array. By dividing the complex array for $\tilde{\rho}$ by the complex array for $\tilde{u}_{\text{xtrack}}$, we derive N PS values and N AR values (so-called "Monte-Carlo results" in this paper) between $\tilde{\rho}$ and $\tilde{u}_{\text{xtrack}}$. In Section 3.2, we explain how we use these N pairs of PS and AR values to solve N possible GW solutions for each TAD event, taking the specific TAD event shown in Figure 1j as an example. Whether a TAD observed in the along-track data set is a GW or not (and if yes, how the GW parameters are distributed) will depend on the distribution of those N GW solutions.

3.2. Solving GWs Using Dissipative Dispersion and Polarization Relations of Thermospheric GWs

When a wave modulates the thermospheric density and wind simultaneously, phase shifts and amplitude ratios in the perturbations of two or more different parameters (e.g., u', w', ρ', and T') can be observed. Those observed perturbations can be used to determine parameters of the wave (e.g., λ_H, λ_z, ω_{Ir}). For example, Gross et al. (1984) estimated the directions of GW propagation within 180° by utilizing the phase shifts and amplitude ratios of O and N_2 perturbations in the data collected by the Atmospheric Explorer-C satellite. Innis and Conde (2002) utilized measurements from the Dynamics Explorer 2 satellite to determine GW propagation directions with an accuracy of within 90°; although their method included compressibility of air, it did not include viscous dissipation. In a later study, Vadas and Nicolls (2012) developed a generalized approach that accounted for full compressibility and realistic molecular viscosity in the GW dispersion and polarization relations, building on the original work by Vadas and Fritts (2005). In this section, we will introduce how to solve the intrinsic parameters of a GW event when it is measured as a TAD event in the density and wind by a satellite that flies through the thermosphere.

According to Vadas and Nicolls (2012), when the background conditions are known, both the sinusoidal perturbations in the relative density ($\tilde{\rho}$, in %) and horizontal wind along the GW propagation ($\tilde{u}_H$, in m/s) caused by a

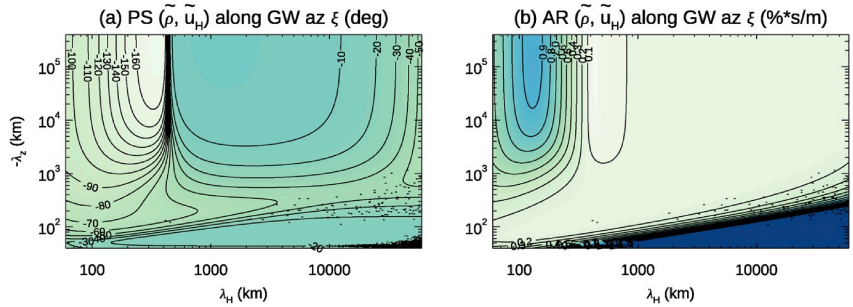

Figure 2. (a) The phase shift between $\tilde{\rho}$ and $\tilde{u}_H$ for gravity waves (GWs) along their propagation direction (contour labels are in unit of degrees). (b) The amplitude ratio between $\tilde{\rho}$ and $\tilde{u}_H$, that is, $|100 * \tilde{\rho}/\tilde{u}_H|$ for the GWs (contour labels are in unit of %*s/m). The background state of the thermosphere is determined by NRLMSIS2.1 for 5 July 2010 at 22:53:00 UTC, 79.43°S, 75.53°E, and $z = 270$ km. (a) and (b) are also visualization of $-F_{\arg}(\lambda_H,-\lambda_z)$ and $|F(\lambda_H, -\lambda_z)|$, respectively, as defined by Equation 1.

GW can be expressed as a function of horizontal and vertical wavelengths (λ_H and λ_z) using the GW dispersion relation and polarization relations. We define their ratio ($\tilde{\rho}/\tilde{u}_H$) as the complex function F:

$$\frac{\tilde{\rho}}{\tilde{u}_H} = F(\lambda_H, -\lambda_z). \tag{1}$$

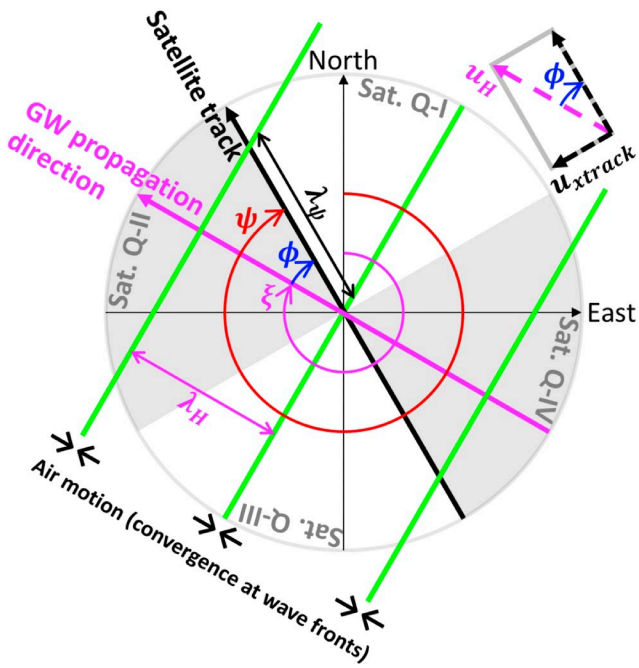

Figure 3. Track of the satellite which is moving with azimuth ψ (thick black arrow), gravity wave (GW) propagation direction (thick magenta arrow with azimuth ξ), $\phi = \psi - \xi$(clockwise from ξ to ψ) and GW lines of constant phase (green parallel lines) in the horizontal plane. $\lambda_H$is the GW horizontal wavelength, defined as the distance between two consecutive GW phase fronts at a fixed moment. λ_ψ is the distance between two consecutive GW phase fronts measured by the satellite along the track at a fixed moment (defined as $\lambda_H = \lambda_\psi * |\cos\phi|$). (Note that λ_ψ and λ_{track} are different because the former quantity is the actual distance between phase fronts after taking into account the Doppler effect, while the latter quantity is the distance between peaks measured by the satellite. Details are contained in Appendix D and Figure D1.) "Sat. Q-I" through "Sat. Q-IV" denotes the 4 Satellite quadrants relative to the satellite flight direction.

Function F includes the dispersion and polarization relation functions over the independent variables λ_H and λ_z. The argument and amplitude function F are denoted as $F_{\arg}$ and $|F|$, respectively. The complete form for function F can be derived using Equations (C2) and (C3) in Appendix C. When both sinusoidal variables $\tilde{\rho}$ and $\tilde{u}_H$ are expressed as phasors, their ratio is a complex variable. The argument ($\arg(\tilde{\rho}/\tilde{u}_H)$) of this ratio is equal to the PS between $\tilde{\rho}$ and $\tilde{u}_H$ but with the opposite sign, and its modulus ($|\tilde{\rho}/\tilde{u}_H|$, in %*s/m) is equal to the AR of $\tilde{\rho}$ and $\tilde{u}_H$. Suppose we want to confirm whether TAD #2 identified in the density perturbation (see TAD #2 Figure 1e) is a GW event or not. The background parameters needed by the function F, such as N_B (buoyancy frequency), c_s (sound speed), $\mathcal{H}$ (density scale height), ν (kinematic viscosity, $\nu = \mu/\overline{\rho}$, where μ is the molecular viscosity), γ (ratio of specific heats), etc., are determined directly or indirectly from the Naval Research Laboratory MSIS (NRLMSIS) 2.1 model (Emmert et al., 2022). This model inputs the time and location for the TAD event. For TAD #2 event shown in Figure 1, (lat, lon) = (79.43°S, 75.53°E) and UTC time = 2010-07-05_22:53:00. Figures 2a and 2b visualize the PS and AR of ($\tilde{\rho}, \tilde{u}_H$) for GWs with different (λ_H, $-\lambda_z$) for the given background. The potential influence of uncertainties in the NRLMSIS2.1 model on GW solutions, as demonstrated by Vadas and Nicolls (2012), is acknowledged. However, the thorough quantification of this uncertainty necessitates a dedicated investigation, which lies outside the scope of the current study.

If GOCE and CHAMP had measured the horizontal wind perturbation $\tilde{u}_H$ directly, then intrinsic parameters like λ_H and λ_z would have been directly determined by measurements of $\tilde{\rho}$ and $\tilde{u}_H$. However, since GOCE and CHAMP only measured the cross-track wind perturbation $\tilde{u}_{\text{xtrack}}$ (the perturbation perpendicular to the satellite track), λ_H and λ_z of the observed GWs cannot be determined directly unless the geometric relationship between the satellite and GW (i.e., the angle between the satellite path and the GW propagation direction in the horizontal plane) is known or determined. Figure 3 illustrates the geometry of a satellite moving at azimuth ψ, and a GW with

horizontal wavelength λ_H propagating at azimuth ξ. We define the angle between the satellite path and the GW propagation direction to be ϕ using $\phi = \psi - \xi$, thus

$$\tilde{u}_{\text{xtrack}} = -\tilde{u}_H * \sin\phi. \tag{2}$$

By plugging Equation 2 into Equation 1 and transforming the coordinate from the GW-based frame (in which $\tilde{\rho}$ and $\tilde{u}_H$ are defined along azimuth ξ) to the satellite-based frame (where $\tilde{\rho}$ and $\tilde{u}_{\text{xtrack}}$ are defined along satellite flight azimuth ψ), we obtain the AR and PS of $\tilde{\rho}$ and $\tilde{u}_{\text{xtrack}}$ as a function G of three variables λ_H, λ_z and ϕ ($\tilde{\rho}/\tilde{u}_{\text{xtrack}} = G(\lambda_H, -\lambda_z, \phi)$). The derivation of the complete form of G is described in Appendix C.

In Figure 3, λ_ψ is the distance between the phase lines of GW along the azimuth ψ at an instant in time ($\lambda_H = \lambda_\psi * |\cos\phi|$), while the along-track wavelength λ_{track} is determined from the peaks in wavelet spectra discussed in Section 3.1 (e.g., Figures 1e and 1g). If we assume that the satellite velocity is infinitely large, then λ_ψ and λ_{track} are identical. However, λ_ψ and λ_{track} differ somewhat due to the Doppler shift (especially for the fast GWs), and their relationship

$$2\pi/(\lambda_\psi * |\cos\phi|) = H(\lambda_{\text{track}}, \phi, U_H) \tag{3}$$

is derived in Appendix D, where U_H is the background horizontal wind along the direction of GW propagation. Since λ_{track} is obtained from the wavelet spectra and U_H is derived from the HWM14 model (Drob et al., 2015), Equation 3 describes the relationship between λ_H and ϕ. (Similar to NRLMSIS2.1, the current study does not contain a quantification of the uncertainty in the HWM14 model. Addressing this limitation is presently beyond the scope of our capabilities.) By plugging Equation 3 and $\lambda_H = \lambda_\psi * |\cos\phi|$ into the function G, the number of unknowns on the right-hand side can be reduced from 3 (λ_H, λ_z and ϕ) to 2 (λ_z and ϕ); thus the function G can be written as $\tilde{\rho}/\tilde{u}_{\text{xtrack}} = G(\phi, -\lambda_z)$, or

$$\begin{cases} \text{PS}(\tilde{\rho}, \tilde{u}_{\text{xtrack}}) = -\arg(G(\phi, -\lambda_z)) \\ \text{AR}(\tilde{\rho}, \tilde{u}_{\text{xtrack}}) = |G(\phi, -\lambda_z)| \end{cases}. \tag{4}$$

The complete form of function G is elaborated in Equation C11 of Appendix C.

The determination of the left-hand side of Equation 4 through the density and cross-track wind observations is explained in Section 3.1; however, solving ϕ and λ_z is still a great challenge due to the computational complexity of linearizing function G within a reasonable processing time for automation purposes. An easier way to address this problem is to make two arrays for the right-hand side of Equation 4 and then utilize the arrays as a pair of "lookup tables" to find the best solution for ϕ and λ_z with given PS and AR of ($\tilde{\rho}, \tilde{u}_{\text{xtrack}}$). Figure 4a visualizes the function -arg($G(\phi, -\lambda_z)$) for the unsolved TAD depicted in Figure 1j based on its background information, and Figure 4b visualizes function $|G(\phi, -\lambda_z)|$. As being discussed in Section 3.1, we obtain $PS(\tilde{\rho}, \tilde{u}_{\text{xtrack}}) = 154.3°$ and $\text{AR}(\tilde{\rho}, \tilde{u}_{\text{xtrack}}) = 0.105$ for TAD wave packet in Figure 1j. By overplotting the green contour for $\text{PS}(\tilde{\rho}, \tilde{u}_{\text{xtrack}}) = 154.3°$ in Figure 4a and orange contour for $\text{AR}(\tilde{\rho}, \tilde{u}_{\text{xtrack}}) = 0.105$ in Figure 4b, we have one solution in Sat. Q-II ($\phi \in (0^\circ, 90^\circ)$) and another solution in Sat. Q-IV ($\phi \in (180^\circ, 270^\circ)$) in $\phi - \lambda_z$ space, meaning that there are two analytical solutions if we assume no uncertainties caused by noise. Then using the red-noise model described in Section 3.1 and Appendix B, we generate 1,000 Monte Carlo values that satisfy the distribution of phasors $\tilde{\rho}$ and $\tilde{u}_{xtrack}$, the accordingly PS values are perturbed around $\text{PS}(\tilde{\rho}, \tilde{u}_{xtrack}) = 154.3°$ and so do AR values around $\text{AR}(\tilde{\rho}, \tilde{u}_{xtrack}) = 0.105$. The 1,000 magenta plus signs in Figures 4a and 4b show the distribution of these solutions with perturbed PS and AR values; 86% of these solutions are in Sat. Q-II ($\phi \in (0^\circ, 90^\circ)$). Therefore, this TAD event (observed by GOCE) is likely a GW event with a position in $\phi - \lambda_z$ space in Sat. Q-II ($\phi \in (0^\circ, 90^\circ)$). Since the satellite movement azimuth is $\psi = -140.7^\circ$ and the peak of $\phi = 43.6°$ (Figure 4c), the azimuth of this GW's propagation direction is $\xi = \psi - \phi = 175.7°$. Figure 4d shows the location (green cross) and simultaneous propagation direction (magenta arrow) of the observed GW overplotted in a map.

Figures 1–4 illustrate the procedure for extracting TADs from along-track GOCE observations and determining if a TAD event represents a GW by solving its most probable intrinsic parameters. In Figures 4a and 4b, the concentration of Monte-Carlo results within Sat. Q-I provides strong evidence that this TAD is a GW. However, a significant fraction of TADs identified through wavelet analysis cannot be confirmed as GWs due to various factors, such as excessive noise leading to overly scattered Monte-Carlo results. To facilitate automation and

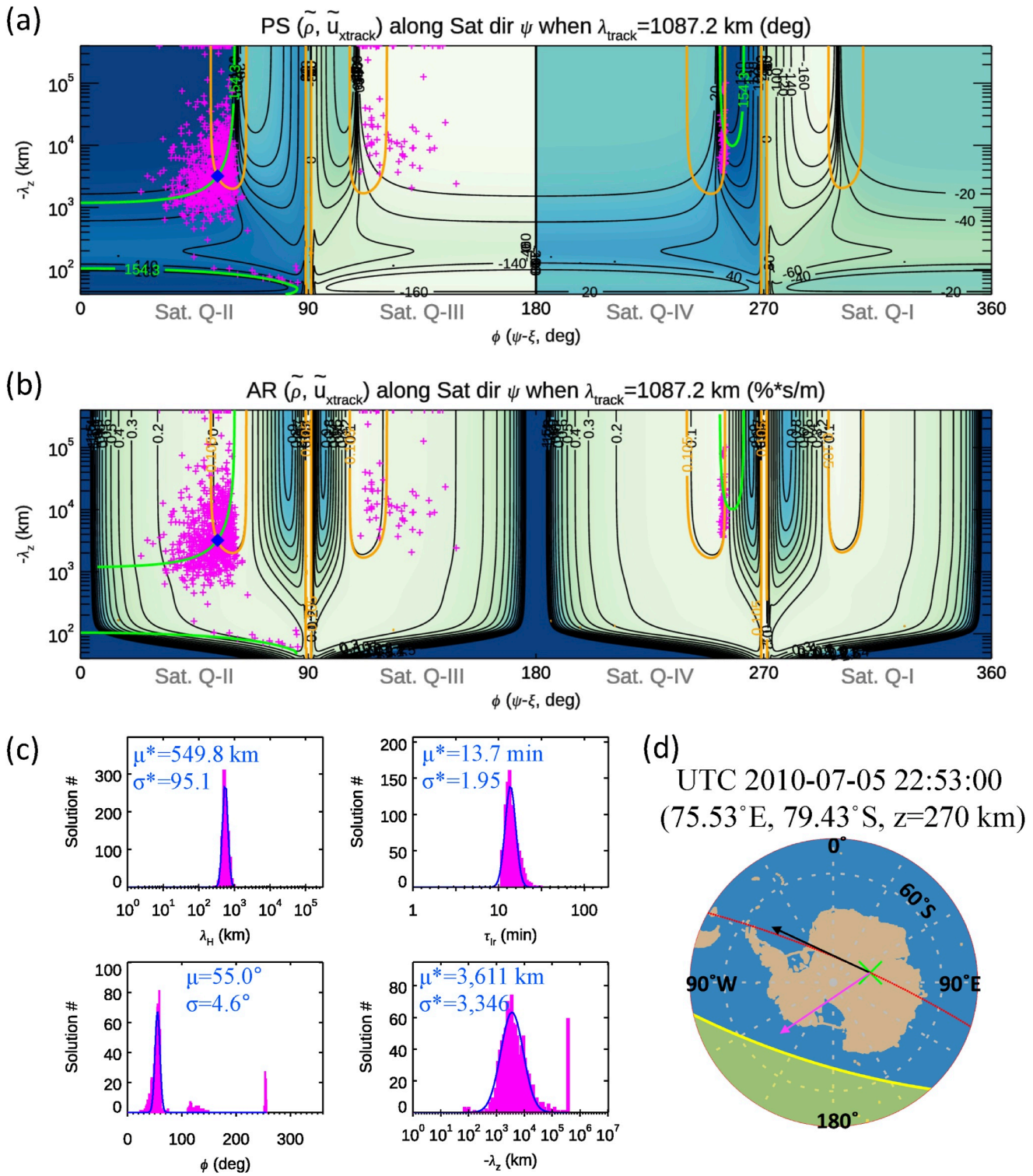

Figure 4. An example of solving a gravity wave (GW) event. (a) Phase shift (unit in degrees) between $\tilde{\rho}$ and $\tilde{u}_{xtrack}$ for a GW detected along the satellite track with λ_{track} = 1,087.2 km as a function of $\phi = \psi - \xi$. (b) The same as (a) but for the GW amplitude ratio $|100 * \tilde{\rho}/\tilde{u}_H|$ (unit in %*s/m). (a) and (b) are also visualizations of $-G_{arg}(\lambda_H, -\lambda_z)$ and $|G(\lambda_H, -\lambda_z)|$, respectively, as defined by Equation 4. Green contours represent PS($\tilde{\rho}, \tilde{u}_{xtrack}$) = 154.3°, and orange contours represents AR($\tilde{\rho}, \tilde{u}_{xtrack}$) = 0.105, without considering any noise in the measurements. Magenta plus signs represent 1,000 Monte-Carlo solutions of $\tilde{\rho}$ and $\tilde{u}_{xtrack}$ that satisfy the red-noise model. The intersection of most Monte-Carlo solutions in Sat Q-II ($\phi \in (0^{\circ}, 90^{\circ})$) are considered the "unperturbed solution" (also optimal solution in this case) and are denoted by blue diamonds. (c) Occurrence frequency distribution of intrinsic GW parameters (λ_H, τ_{lr}, ϕ, λ_z) derived from the 1,000 Monte-Carlo solutions (purple). The blue curves are Gaussian (ϕ) or log-normal (λ_H, τ_{lr}, λ_z) fits to each histograph. (d) Data points along the satellite track (red dots), location of the observed GW (green cross), the direction of satellite motion (black arrow), and the direction of the GW propagation obtained by the peak of ϕ in (c) (lower left).

Table 1
Criterion Required to Determine if a Traveling Atmospheric Disturbance Event Is a Gravity Wave Event

Category	Criterion	Notes
Solution check	(Unperturbed PS in solution/observed PS) ∈ (1 ± 30%) AND Unperturbed AR in solution ∈ (observed AR ± 30°)	For some TAD events that are not GWs, it is impossible to have a GW solution because there is no PS or AR values in "lookup tables" that are close to PS or AR values derived from observation, but our program still returns a solution. We set these criteria to prevent those cases from being counted as solvable GWs.
General distribution	Percent of GW solutions in Monte-Carlo tests >60%	If there are too many (>40%) Monte-Carlo tests that do not return GW solutions, then the Monte-Carlo tests are considered invalid
General distribution	Percent of GW solutions in one Sat. $Q > 60\%$	If GW solutions provided by Monte-Carlo tests are overly spaced-out in different satellite quadrants, then the Monte-Carlo tests are considered invalid
λ_H	Unperturbed solution ∈ (Gaussian fit center ± Gaussian fit standard deviation)	GW solutions provided by the Monte-Carlo tests should show a good concentration that are aligned to the unperturbed solution.
τ_{lr}	Same as previous row	Same as previous row
ϕ	Same as previous row	Same as previous row
λ_H	Unperturbed solution of $\lambda_H > 50$ km	Lower limit for reliable λ_H solutions, since the 10 s sampling cadence corresponds to ∼80 km along-track distance for GOCE and CHAMP.
τ_{lr}	Unperturbed solution of $\tau_{\mathrm{lr}} > 5$ min	Lower limit since τ_{lr} > the buoyancy period τ_B, which is > 5 min in the thermosphere
ϕ	Standard deviation of $\phi < 30°$	
ϕ	Unperturbed solution ∉ (70°, 110°) and ∉ (250°, 290°)	The contours of $-G_{\mathrm{arg}}$ and G_{mod} at ϕ near around 90° or 270° is very dense (Figure 4), so it is easy to get a ϕ solution with large uncertainty. Additionally, according to equation $\lambda_H = \lambda_\psi \lvert\cos\phi\rvert$ (Figure 3), even a small uncertainty in ϕ can induce a large uncertainty in λ_H when ϕ is around 90° or 270°.

enable statistical analysis, we have established criteria in the code for assessing whether an observed TAD event qualifies as a GW. In Table 1, we present the criteria that must be satisfied for an event to be classified as a GW. This approach aids in streamlining the process and facilitating comprehensive statistical investigations. The flowchart in Appendix E shows the data processing procedure.

4. Results and Discussion

We now extract TADs and identify GWs in each orbit of GOCE (November 2009 to October 2013) and in CHAMP (2004–2007) during quiet time using the process described in Section 3. By "quiet time" we mean GW events that occurred when both the concurrent Kp and the average Kp over the past 6 hr were less than 3 in order to minimize the waves from geomagnetic disturbances. Figure 5a shows the number of TAD (gray) and GW (green) events we identified from the GOCE data during each month in 2011. During this year, the total number of GOCE TAD and GW events are 206,225 and 34,378 respectively; therefore, only ∼17% of the TAD events were GW events with relatively high confidence. For the GOCE observations during 2009–2010 and 2012–2013, the ratio of GW events identified from TAD events are similar (∼17%, not shown). Although some of the TADs are not GWs (e.g., terminator waves, etc.), other adverse conditions that prevent us from identifying GWs include but are not limited to: (a) The wavelet spectrum of a TAD wave packet can be very wide, thus making it difficult to determine the correct values of the dominant λ_{track} and amplitudes for that wave packet. (b) The noise level from the red-noise model may have been overestimated for some GW events, yielding GW solution below the confidence threshold. (c) When the solution of a GW is close to ϕ ∼0° or 180°, it is relatively easy to measure waves in the density but almost impossible to extract cross-track wind perturbations because the amplitude is quite small. (d) When a solution has $\phi \sim 90°$ or 270°, it is challenging to derive reliable GW parameters (see last row of Table 1). Therefore, the low percentage of GWs extracted from the TADs shows the limitation of our method, and should be interpreted as "at least 17% of TAD events observed in GOCE are GWs." Figure 5b shows the analogous results for CHAMP data for the year 2006. For this year (and other unillustrated years), approximately 11% of the observed TAD events are identified as GW events. This lower GW occurrence in CHAMP is potentially attributed to two factors: (a) CHAMP's observations have more noise than GOCE due to less precise accelerometers and lower density (higher altitude), thereby contributing to larger uncertainties in solved parameters following the Monte-Carlo tests; (b) the lower percentage of GWs may be geophysics due to the higher

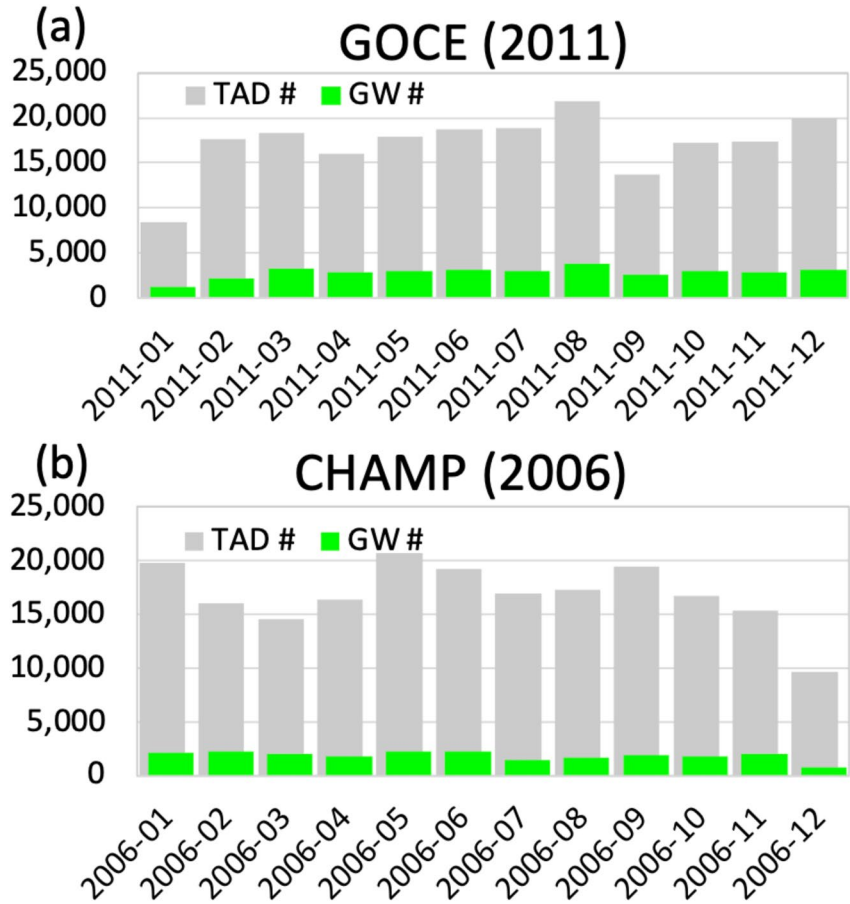

Figure 5. (a) Number of GOCE traveling atmospheric disturbance (TAD) events identified each month in 2011 (gray) alongside gravity wave (GW) events (green). The total count of TAD and GW events are 206,225 and 34,378, respectively. (b) The same as (a) but for CHAllenging Minisatellite Payload TADs and GWs during 2006, with a total of 202,213 TAD events (gray) and 22,270 GW events (green).

altitude of CHAMP (370 km). The quantification of the roles these two factors play in GW percentages within TADs necessitates further investigations targeting the non-GW TADs.

Figure 6 provides a comprehensive overview of the GW characteristics during quiet times as observed by GOCE (left column) and CHAMP (right column). In scatter plots in the top two rows in Figure 6, the c_{IH}–τ_{Ir}–λ_H relationship generally conforms to GW dissipative theory (Vadas & Crowley, 2010). The first row shows c_{IH} versus λ_H. Two populations of GWs are apparent: the first population (with the largest # of GWs) has $c_{IH} > 300$ m/s and $\lambda_H \sim 200$ km to thousands of kilometers while the second population has $c_{IH} < 300$ m/s and $\lambda_H < 500$ km. Thus the first population contains medium (100 km $< \lambda_H <$ 1,000 km) to large-scale ($\lambda_H >$ 1,000 km) GWs. Note that for each population, c_{IH} is proportional to λ_H, similar to previous results (Vadas & Crowley, 2010). The second row shows a scatter plot of τ_{Ir} versus λ_H. The two populations are again apparent here, although both populations have $\tau_{Ir} \sim 10$–50 min. The third to fifth rows show the number of GWs as a function of λ_H, c_{IH}, and τ_{Ir} respectively, with histograms in red and Gaussian fits in blue. There are many more GW events in the first than in the second population. The first population has a peak horizontal wavelength, intrinsic horizontal phase speed and intrinsic period of $\lambda_H = 585$ km, $c_{IH} = 688$ m/s and $\tau_{Ir} = 14.3$ min for the GOCE GWs and $\lambda_H = 655$ km, $c_{IH} = 768$ m/s and $\tau_{Ir} = 14.4$ min for the CHAMP GWs, respectively. The second population has a broad distribution of $\lambda_H = 100$–400 km and peaks at $c_{IH} = 100$–250 m/s with smaller (but still significant) amplitudes as compared to the first population in the GOCE data. From the CHAMP data, however, the amplitude of the second population is quite small as compared with that of the first population. This implies that the GWs in the second population have dissipated between 250 and 350 km; this is the expected behavior, because the GWs in the first population (having $c_{IH} < 300$ m/s and $\lambda_H < 500$ km) dissipate rapidly in the vicinity of (or below) $z \sim 250$ km

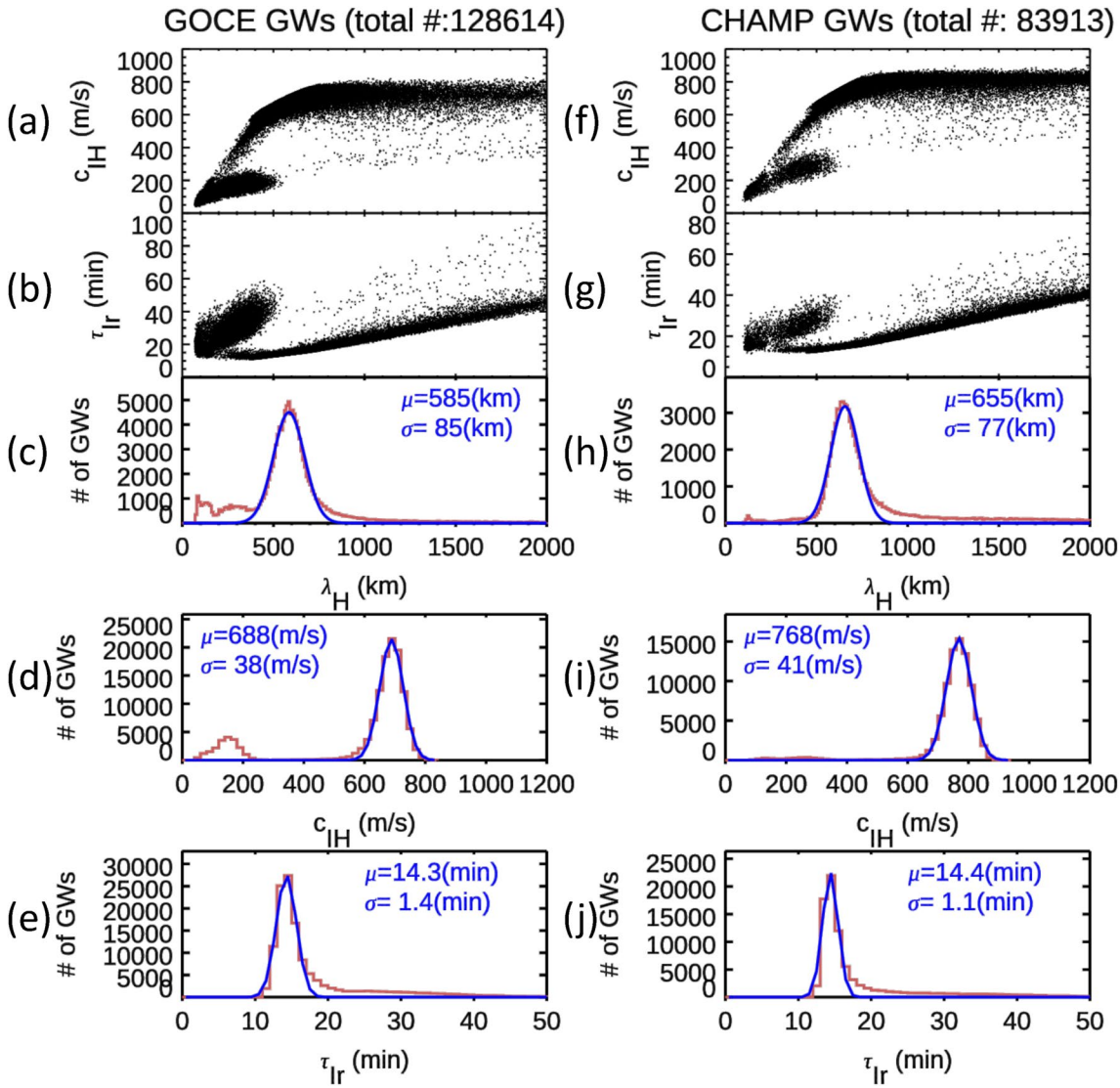

Figure 6. Attributes of all gravity wave (GW) events observed by GOCE (left column) and CHAllenging Minisatellite Payload (CHAMP) (right column). The total number of identified GW events is given at the top of each column. (a) Scatter plot of intrinsic phase speed c_{IH} versus horizontal wavelength λ_H; (b) Scatter plot of intrinsic period τ_{Ir} versus λ_H; (c), (d), and (e) represent the number of GW events as a function of λ_H, c_{IH} and τ_{Ir}, respectively (red histograms). Gaussian fits are provided for (c–(d) (blue lines) with the μ (mean) and σ (standard deviation) given in each panel. (f–g) The same as left column (a–e) but for GWs observed in CHAMP.

due to the rapidly increasing kinematic viscosity with height, according to ray trace results (Figures 4–7 of Vadas (2007)).

In the third row of Figure 6, the distribution of the horizontal wavelengths λ_H of the GWs in the first population approximate a Gaussian distribution, with most of the GWs having $\lambda_H \sim$ 400–800 km. R. F. Garcia et al. (2016) noted that most of the GOCE GW signal occurred in a spectral range above 8 mHz, corresponding to a maximum horizontal wavelength along the satellite track of around 1,000 km. Since their "horizontal wavelength" in that statement is equivalent to λ_{track} in our study, because $\lambda_H \approx \lambda_{track} * |cos\phi|$ (where we have simplified by ignoring the Doppler's effect such that $\lambda_{track} \approx \lambda_\psi$), and since $|cos\phi| \sim 0.71$ for a typical TAD in our study (since our typical TAD has $\phi \sim 45^\circ$), their statement is equivalent to $\lambda_H \approx$ <710 km. This agrees with our results shown in Figures 6c and 6h.

The horizontal phase speeds of the GWs in the first population are c_{IH} ~600–800 m/s (GOCE) and 650–850 m/s (CHAMP). In a study by Bruinsma and Forbes (2009), an investigation was conducted on 21 TAD events originating from the auroral zone and propagating across multiple CHAMP orbits into the opposite hemisphere.

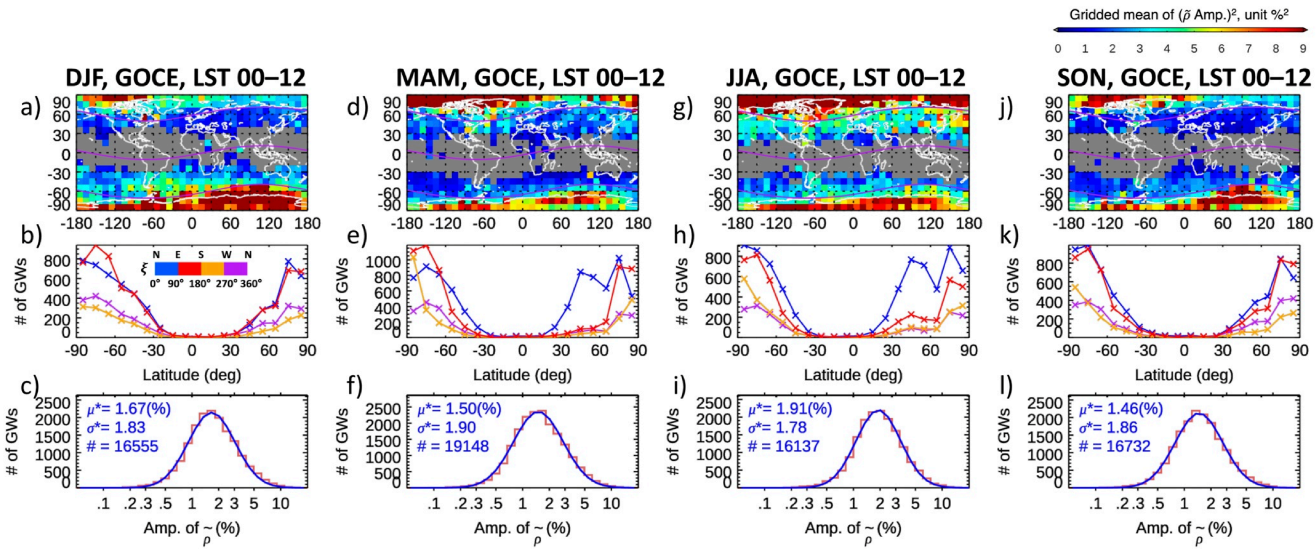

Figure 7. Statistical results based on gravity waves (GWs) observed by GOCE during 0–12 local solar time during November 2009 to October 2013. Each column shows the GW events in four different seasons: DJF (December-January-February), MAM (March-April-May), JJA (June-July-August), and SON (September-October-November), respectively. (a) Global distribution of gridded mean GW intensity or $\sum_i (\text{Amp. of } \tilde{\rho}_i)^2 / N$, where (Amp. of $\tilde{\rho}_i$) represents the relative density amplitude (unit %) of an identified GW event and N is the total number of identified GWs in a 10° × 10° map grid. Gray grids indicate regions with less than 3 GW events. The purple curves in maps depict the geomagnetic latitude of 60°, 0°, and −60°. (b) Number of GW events in four different propagation direction quadrants as a function of latitude. The blue curve corresponds to $0° < \xi < 90°$, the red to $90° < \xi < 180°$, the orange to $180° < \xi < 270°$, and the purple to $270° < \xi < 360°$. (c) The number of GW events as a function of the relative density amplitude (Amp. of $\tilde{\rho}$) (red histograms). Note the logarithmic scale on the horizontal axes. Gaussian fits (blue), and the fit parameters μ^* (multiplicative mean) and σ^* (multiplicative standard deviation) are displayed in each panel (blue). (d–f) show the same analysis as (a–c) but for the MAM season. (g–i) show the same analysis as (a–c) but for the JJA season. (j–l) show the same analysis as (a–c) but for the SON season.

Their findings indicate an average speed of 646 ± 122 m/s for all TADs, which agrees with the phase speeds of most of the GWs resolved in our analysis. The horizontal phase speeds of these GWs are so large that they could not have propagated from the lower/middle atmosphere. This is because a GW can only propagate in the lower/middle atmosphere if $c_{\text{IH}} \leq 0.9\, c_s$, where c_s is the sound speed ($c_s \simeq 310$ m/s) in the lower/middle atmosphere (Vadas et al., 2019). Therefore, no GW with $c_{\text{IH}} \geq 300$ m/s could have propagated from the lower/middle atmosphere to GOCE/CHAMP altitudes, while the GWs in the second population could have propagated from the lower/middle atmosphere to GOCE/CHAMP altitudes. Therefore, we speculate that the GWs in the second population could be mainly primary GWs from high-frequency lower/middle atmospheric sources (such as deep convection), while the GWs in the first population are likely 1) higher-order GWs from the dissipation of GWs from the lower/middle atmosphere (e.g., from deep convection, the polar vortex, orographic forcing, jet and fronts (Becker, Goncharenko, et al., 2022; Becker & Vadas, 2020; Vadas & Becker, 2019)) and/or 2) GWs from Joule heating in the thermosphere (Hocke & Schlegel, 1996). Secondary GWs from Tropical Storm Noel, determined via reverse ray-tracing, were observed at z∼280 km at Wallops Island, VA as TIDs on 30 October 2007 with λ_H = 100–2,000 km, c_{IH} = 140–600 m/s and τ_{Ir} = 20–60 min (Vadas & Crowley, 2010). These GWs are consistent with our first and second population results. Waldock and Jones (1986) observed medium-scale traveling ionospheric disturbances (MSTIDs) over the UK using HF Doppler sounding technique. They found that the observed MSTIDs had horizontal phase speeds of $c_H \sim 50-350$ m/s (with a peak at $c_H \sim 140-150$ m/s) and periods of $\tau_r \sim 10-55$ min (with a peak at $\tau_r \sim 15-20$ min). These GWs agree well with the second population of GWs observed by GOCE in Figure 6.

Using the parameters we identified for the GOCE GW events, we present the statistical results during four different seasons for 0–12 LST (Figure 7) and 12–24 LST (Figure 8). The first row of Figures 7 and 8 illustrates the global distribution of 10° × 10° lat-lon gridded mean GW intensities for various seasons. These maps show clear seasonal and LST dependence of the GW intensity. Note that the gray shading (mostly at low latitudes) display pixels containing less than 3 GW events. The summer polar regions exhibit the strongest GW intensities. In addition, at 0–12 LST, moderately strong GW intensity is observed at the summer mid-latitudes (60°S–30°S in Figure 7a and 30°N–60°N in Figure 7g). Since there is no clear geographic concentration for these GWs (i.e., no apparent concentration at specific longitudes), it is not apparent whether these mid-latitude GWs originate from

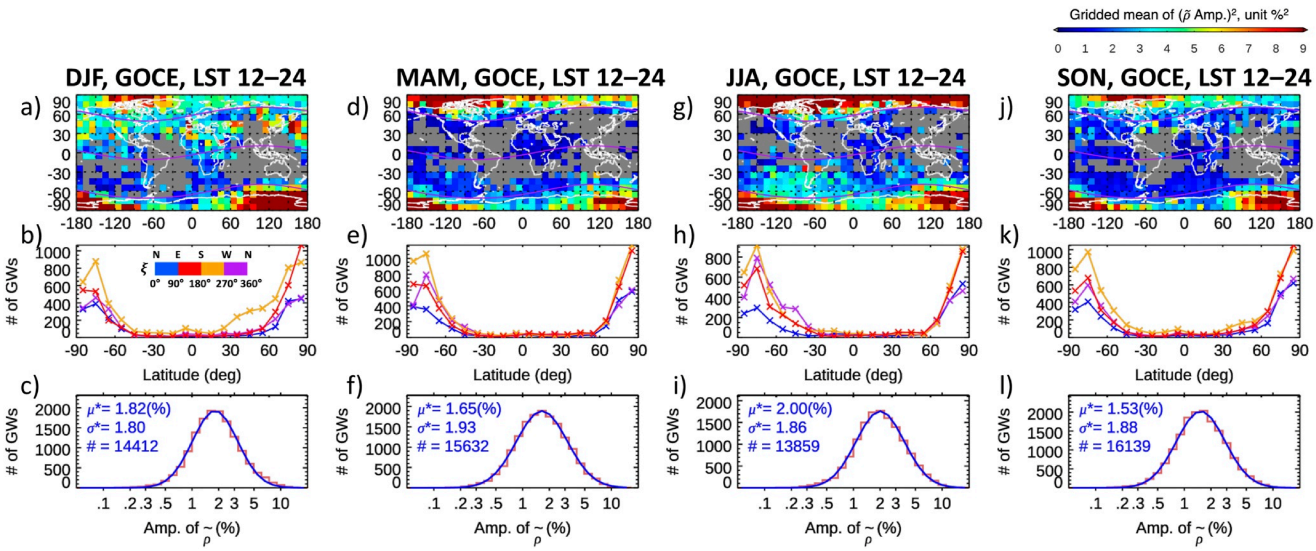

Figure 8. The same as Figure 7 but for gravity waves observed by GOCE during 12–24 local solar time.

local or low-latitude deep convection or are generated from the polar regions and propagate to mid latitudes. In contrast, at 12–24 LST, the GW intensities are not significantly strong at summer mid-latitudes. However, their distribution closely aligns with the location of deep convection (e.g., the African sector and North America during the local summer season in Figure 8). We explain the LST dependence of GWs from deep convection below. During the southern hemisphere wintertime for any LST, there is an increase (over the background) of GWs over and near the Southern Andes and Antarctic Peninsula at 60°S–30°S in Figures 7 and 8g (Trinh et al., 2018; Xu et al., 2021). In addition, we note that the so-called "background" distribution is quite wide in latitudinal extent (to ∼20°S) and occurs for most longitudes, thereby suggesting that the polar vortex is also a source of higher-order GWs in the winter southern thermosphere at mid to high latitudes (Becker, Vadas, et al. (2022) explored these GWs using a model and data in the northern winter thermosphere). During the northern hemisphere winter at 30°N–60°N, there is a significant increase (over the background) of GWs over the Continental United States and Greenland at 0–12 LST (Figure 7a) and even more so at 12–24 LST (Figure 8a). In addition, the "background" here also spans a wide latitudinal extent (to ∼20°N) and also covers most longitudes, thereby suggesting that the polar vortex is also a source of higher-order GWs in the winter northern thermosphere at mid to high latitudes (Becker, Vadas, et al., 2022; Vadas, Becker, Bossert, et al., 2023). Thus our observations suggest that (a) orographic forcing is an important source of higher-order GWs in the winter hemisphere, and (b) the polar vortex might be an important source of higher-order GWs in the winter hemisphere. Note that although Becker and Vadas (2020) modeled the GW hotspots during the northern and summer winter thermosphere, they attributed those hotspots as due mainly to tertiary GWs from orographic forcing; however, it is possible that some of those GWs may have instead been higher-order GWs from the polar vortex.

The second row of Figures 7 and 8 depicts the statistical analysis of GW propagation direction ξ, and the third row shows relative density amplitude (Amp. of $\tilde{\rho}$). The GWs in the winter and summer polar regions clearly have the largest amplitudes. We now summarize important similarities between Figures 7 and 8:

1. GW hotspot patterns occur near both geographic poles with boundaries parallel to the geomagnetic latitudes 60°S and 60°N (purple) in the first rows, especially in the polar summer season.
2. The strongest GW intensities occur in the polar summer regions (first row). Additionally, the mid- and low-latitude regions (60°S–60°N) generally exhibit stronger GW activities during solstice seasons (DJF and JJA) than in the equinox seasons (MAM and SON). The low-latitude regions (30°S–30°N) typically exhibit a very low number of TAD events that are observable/solvable with our method.
3. The high latitudes have significantly higher numbers of GW events compared to mid and low latitudes (second row).
4. Most of the GWs have density amplitudes within the range of 0.5%–5 % (third rows). Intriguingly, all density amplitude histograms exhibit a log-normal distribution (third row). While prior research by Bezděk (2007)

and Doornbos (2012) observed a log-normal distribution consistent with the ratio of accelerometer-derived densities and empirical model densities, they attributed this pattern to the multiplication of random errors, such as the satellite frontal area and drag coefficient (Doornbos, 2012). Given the ubiquity of log-normal distributions in natural phenomena (Limpert et al., 2001), unraveling the specific underlying characteristics of GWs in the thermosphere, as observed here and in other thermospheric perturbations, may warrant further inquiry to elucidate the log-normal distributions observed in these earlier investigations.

Noticeable differences also occur between Figures 7 and 8, especially in the low- and mid-latitude regions (60°S–60°N):

1. In the tropical regions, the GWs at 12–24 LST are stronger than those at 0–12 LST (first rows of Figures 7 and 8), although neither are as intense as at higher latitudes. This LST dependence likely indicates that these GWs are primary or higher-order GWs from deep convection, since deep convection has a strong local time dependence (strongest during the afternoon through local time midnight) because direct solar heating (and evaporation of water) is generally required for the atmosphere to become convectively unstable (Cotton & Anthes, 1992). Our results are consistent with Bruinsma and Forbes (2008), who found a strong LST dependence of the quiet time TADs identified from CHAMP data, with the largest amplitudes occurring for λ_{track}~1,400–2,400 km at 16:00–4:00 LST. The tropical GWs at 12–24 LST are mainly concentrated near the Pacific-America and Africa sectors, corresponding to two of the peaks in the "three-peak longitudinal structure in tropics" reported in H. Liu et al. (2017). (These 3 peaks are likely related to the 3-peaked occurrence and strength of deep convective plumes in tropical regions (Vadas et al., 2014).) However, we did not observe the weakest peak from Liu's paper, which is located in the Asian-Maritime Continent sector. The absence of these GWs in our results can be attributed to their small amplitudes in both density and cross-track wind, falling below our required 95% confidence threshold using the red-noise model. This discrepancy suggests that our assumed noise model used for GW identification may be overly conservative for identifying GWs.
2. In the second row of Figure 7, the blue curve ($0° < \xi < 90°$) is generally the highest, and the red curve ($90° < \xi < 180°$) is the second-highest component for 0–12 LST. This indicates that most GOCE GWs have a propagation direction with an eastward component during this period. However, in the second row of Figure 8, either the orange curve ($180° < \xi < 270°$) or the purple curve ($270° < \xi < 360°$) is highest, suggesting that most CHAMP GWs have a propagation direction with a westward component during 12–24 LST.
3. Figures 7a and 7g demonstrate that at mid-latitudes, the summer hemisphere exhibits stronger GWs than in the winter hemisphere during 0–12 LST. Conversely, Figures 8a and 8g illustrate that at mid-latitudes, the winter hemisphere exhibits stronger GWs than in the summer hemisphere during 12–24 LST.

Further discussion on the variation of GW propagation directions and interhemispheric differences will be provided in the text related to Figures 11 and 12.

Figures 9 and 10 show the same results as Figures 7 and 8, except for the CHAMP GWs during January 2004 to December 2007 (z~370 km). Distinct similarities and noteworthy differences between the CHAMP and GOCE GWs (Figures 7 and 8) occur. Similarities between the GOCE and CHAMP results are summarized as follows:

1. Across the same LST range and seasons, the spatial distribution of the GOCE and CHAMP GWs are similar. As for the GOCE GWs, the polar regions consistently demonstrates higher GW intensities and event counts for the CHAMP GWs than at mid and low latitudes (first and second rows of Figures 9 and 10).
2. Similar to the GOCE GWs, the CHAMP GWs also exhibit predominant eastward and westward propagation directions during 0–12 LST and 12–24 LST, respectively (second rows of Figures 9 and 10).
3. Strong GW hotspots with boundaries roughly aligned with the geomagnetic latitudes of 60°S and 60°N (purple) are observed during the polar summer seasons in both GOCE and CHAMP results.

The third point suggests that GW events with substantial amplitudes are attributable to Joule heating, even during geomagnetic quiet time. This appears to contrast with Xu et al. (2021), which found that quiet time thermospheric TADs observed by GOCE and CHAMP during austral winter were predominantly induced by orographic waves and related higher-order GWs, rather than by geomagnetic activity. However, the definition of "TADs" in Xu et al. (2021) encompassed along-track perturbations spanning 160 km $< \lambda_{track} <$ 2,100 km, regardless of their density amplitude. In contrast, our current study employs a filtering mechanism that may exclude GWs with relatively smaller amplitudes that do not surpass the 95% threshold defined by the red-noise model. This filtering approach could potentially skew our results in favor of larger-amplitude GWs from geomagnetic activity over the

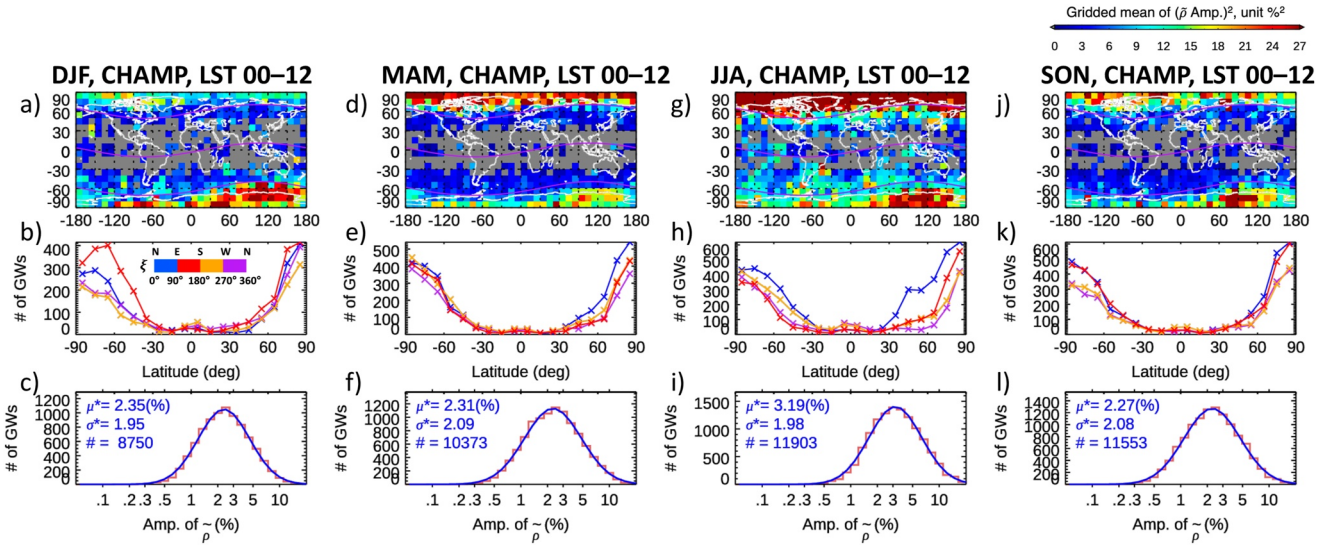

Figure 9. The same as Figure 7 but for gravity waves observed by CHAllenging Minisatellite Payload during 2004–2007 (0–12 local solar time). Note that the color bar range is larger than that for GOCE in Figures 7 and 8.

polar regions, thereby de-emphasizing those somewhat smaller-amplitude GWs over the Southern Andes region. Additionally, while Xu et al. (2021) considered TADs with λ_{track} ranging from 160 to 2,100 km, our study includes GWs with λ_H from 50 to 3,000 km. It is possible that the quiet time aurora generates sizable large-scale GWs (e.g., $\lambda_H > 1{,}500$ km), which might have been filtered out in Xu et al. (2021) but appear as hotspots in our findings. Therefore, the results of our study do not contradict the conclusions from Xu et al. (2021).

Differences between GOCE and CHAMP results shown in Figures 7–10 are:

1. The intensity (or relative density amplitude) of the GWs observed by CHAMP are generally larger than that observed by GOCE (see the color bars and histograms in the third rows).
2. While GOCE only identifies pronounced tropical GW clusters near the Pacific-American and African sectors, CHAMP records elevated intensities and occurrences of equatorial GWs across both 0–12 LST and 12–24 LST. Specifically, the number of GW events around the equator outnumber those at latitudes of 30°S and 30°N (compare the second rows of Figures 7–10).

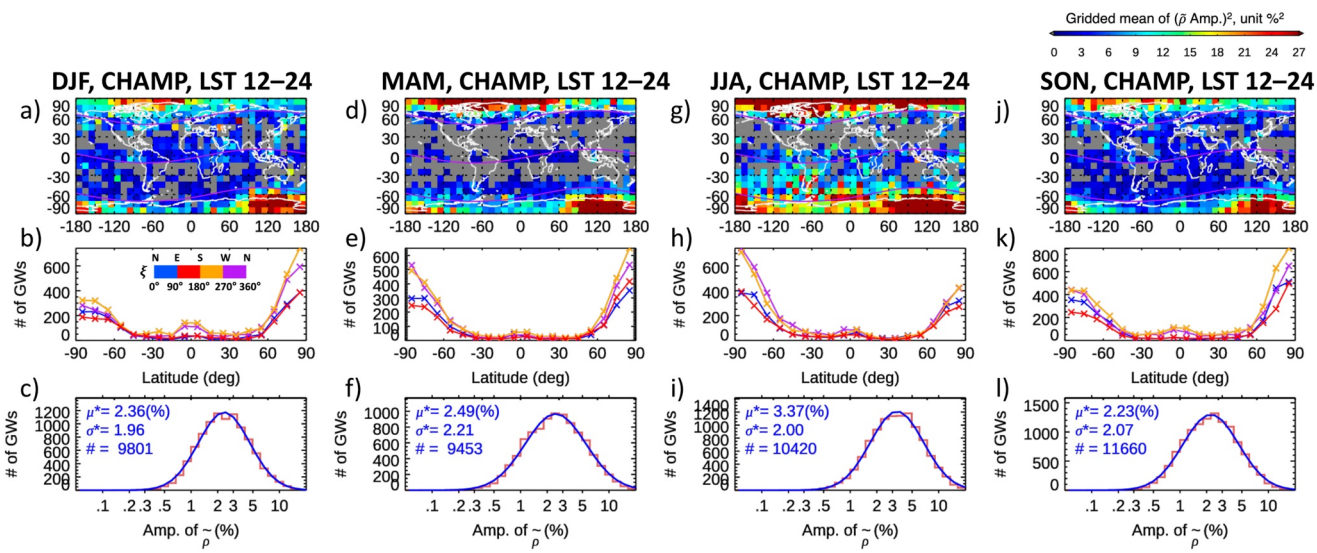

Figure 10. The same as Figure 8 but for gravity waves observed by CHAllenging Minisatellite Payload during 2004–2007 (12–24 local solar time).

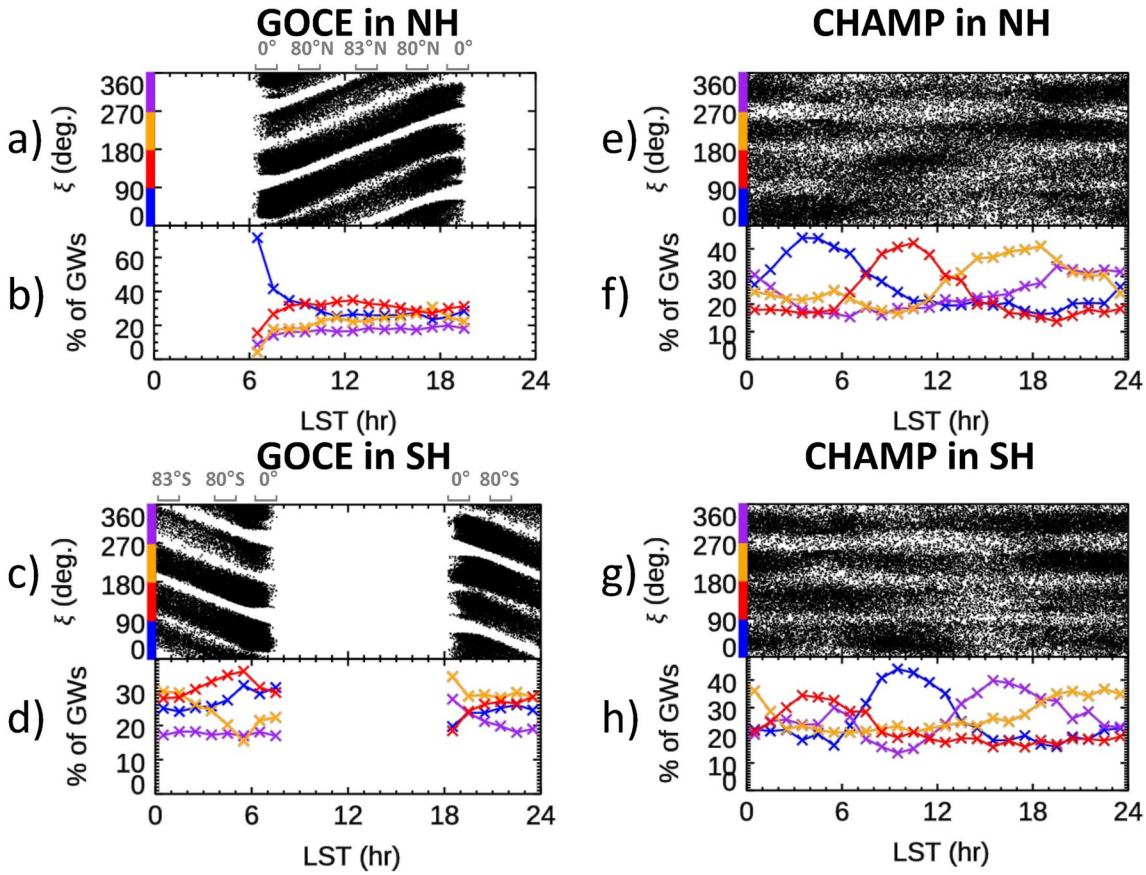

Figure 11. (a) Scatter plot depicting the azimuthal gravity wave (GW) propagation direction ξ as a function of local solar time (LST) for GOCE GWs (2009–2013) within the northern hemisphere. Each data point represents an individual GW event. (b) The distribution of GW events across the four ξ quadrants binned as a function of LST. The blue curve corresponds to $0° < \xi < 90°$, red to $90° < \xi < 180°$, orange to $180° < \xi < 270°$, and purple to $270° < \xi < 360°$. Panels (c) and (d) adopt the configuration of (a) and (b) but for GOCE GWs within the southern hemisphere. (e–h): The same as (a–d) but for the CHAMP GWs (2004–2007). Because of the quasi-fixed local time of GOCE's orbit during 2009–2013, the LST of GOCE's measurements along orbit are highly dependent on latitude. To show this dependency, gray approximated latitude markers are added above the upper *y*-axis in panels (a) and (c).

3. In contrast to the GOCE results, where the solstice seasons (DJF and JJA) exhibit expanded coverage and intensified GWs compared to the equinox seasons (MAM and SON), CHAMP records a unique pattern. In the CHAMP data, the southern hemisphere experiences the strongest GWs during the southern winter season (JJA), resulting in generally heightened intensities across all latitudes in JJA. The largest intensities occur for GWs over and downwind of the Southern Andes/Antarctica Peninsula region.

These 3 differences between CHAMP and GOCE can be attributed to various factors. The altitude difference between CHAMP (~370 km during 2004–2007) and GOCE (~270 km during 2009–2013) accounts for the difference in the GW intensities. As non-dissipating GWs propagate upward, their amplitudes amplify exponentially in altitude (Hines, 1960). The difference in the second point might stem from the dissipation of tropical convectively excited GWs and the generation of higher-order GWs at z~180–200 km, which have more exponential amplitude growth when reaching CHAMP altitudes (Vadas & Liu, 2009, 2013). Or it may be due to the interhemispheric propagation of larger-scale polar-sourced GWs (Bruinsma & Forbes, 2009). For the difference in the third point, further exploration of multiple factors is provided in Figure 12 and the accompanying text.

We now investigate the propagation direction of the GOCE and CHAMP GWs as a function of LST. In particular, significant differences are seen in the GW propagation direction ξ between 0 and 12 LST and 12–24 LST in the middle rows of Figures 7–10; for both GOCE and CHAMP, most GWs have propagation directions with an eastward and westward component during 0–12 LST and 12–24 LST, respectively. In Figure 11 we show a more complete relationship between ξ and LST. Figure 11a shows a scatter plot of ξ and LST for all GW events in the northern hemisphere at 0°–90°N. To see the dominant GW propagation direction more clearly, we divide ξ into

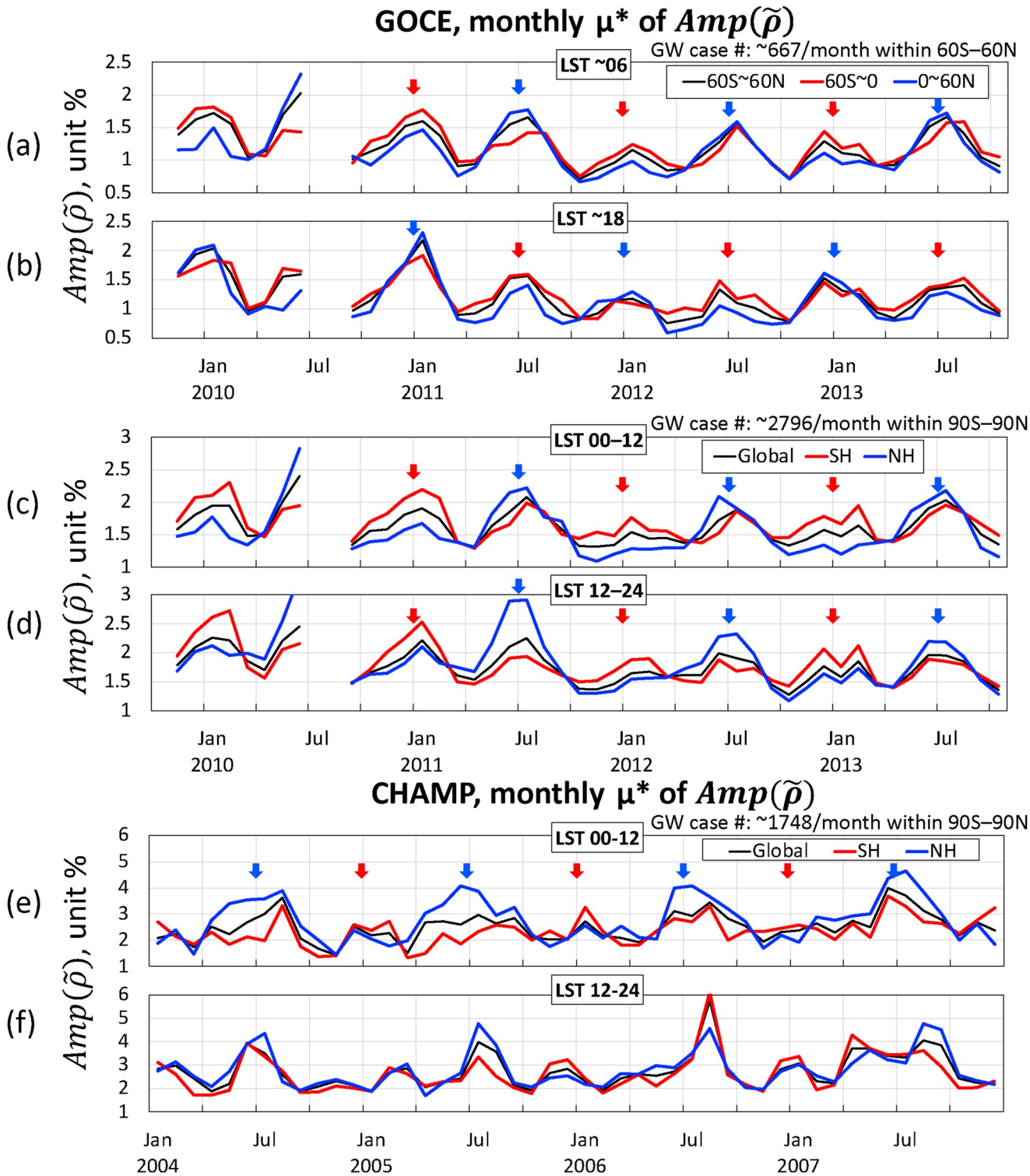

Figure 12. (a–b) Time series of monthly multiplicative mean (i.e., log-normal fitted peak values μ^*). of the relative density amplitude of gravity waves (GWs) (in %) at latitudes of 60°S–60°N (black), 60°S–0° (red) and 0°–60°N (blue). (a)/(b) shows results for GWs at 0–12/12–24 local solar time, respectively. (c–d) Same as (a–b) but for GOCE GWs at all latitudes (black), in the southern hemisphere (red) and in the northern hemisphere (blue). (e–f) Same as (c–d) but for CHAllenging Minisatellite Payload GWs at all latitudes (black), in the southern hemisphere (red) and in the northern hemisphere (blue). Thick arrows at January and July indicate which hemisphere has the higher mean μ^*, with red/blue arrows for the southern/northern hemisphere.

four quadrants (blue, red, orange, purple for $\xi \in (0°,90°)$, (90°,180°), (180°,270°), (270°,360°), respectively) and bin hourly in 24 LST bins. Figure 11b shows the percentage of GW events having azimuths within these 4 different ξ quadrants as a function of LST. Figures 11c and 11d shows ξ versus LST for GWs observed by GOCE in the southern hemisphere at 90°S–0°. As mentioned in Section 2, the LST of GOCE is 6:13–7:33 during the descending nodes and 18:13–19:33 during the ascending nodes, so the LST of GOCE's measurements are highly dependent on latitude. Some LST dependence of ξ is visible for certain LSTs. For example, around 6 LST in the northern hemisphere, the percentage of GWs with $0° < \xi < 90°$ (blue) decreases, while that for GWs with $90° < \xi < 180°$ increases (see Figure 11b). The trend is opposite right after 6 LST in southern hemisphere (see Figure 11d). However, it is difficult to determine how the GOCE GW ξ depends on LST due to the limited LST range.

Figures 11e–11h show the corresponding results for the CHAMP GWs. Because CHAMP orbit drifted rapidly, CHAMP covered all LST. However, because of CHAMP's nearly 90° inclined orbit (87°), there are subtle yet discernible gaps in the data in Figures 11e and 11g near $\xi \sim 0°$, 90°, 180°, and 270°. These characteristic gaps closely align with the gaps from our analysis method, since our method does not solve for GWs that propagate parallel or perpendicular to CHAMP's mostly north/southward tracks. From Figure 11f, during LST of 1–7 hr/7–13 hr/13–20 hr/20–1 hr, the GW azimuths are $0° < \xi < 90°$ (blue)/$90° < \xi < 180°$ (red)/$180° < \xi < 270°$ (orange)/$270° < \xi < 360°$ (purple), respectively. In contrast, Figure 11h shows that during LST of 2–7 hr/7–13 hr/13–19 hr/19–2 hr, the GW azimuths are $90° < \xi < 180°$ (red)/$0° < \xi < 90°$ (blue)/$270° < \xi < 360°$ (purple)/$180° < \xi < 270°$ (orange), respectively. Therefore, the GW propagation direction in northern and southern hemispheres clearly show a strong clockwise and counterclockwise rotation in a local day, respectively. This is the expected result, because the GWs that can best survive dissipation and critical level filtering propagate in a direction opposite to the background wind (Becker, Goncharenko, et al., 2022; Becker, Vadas, et al., 2022; Fritts & Vadas, 2008; Waldock & Jones, 1984). Since the background thermosphere wind (due mainly to the diurnal migrating tide from extreme ultraviolet EUV heating at these altitudes) rotates clockwise (counterclockwise) in the northern (southern) hemisphere (Cowling et al., 1971), clockwise (counterclockwise) rotation of the GWs is expected to occur in the northern (southern) hemisphere. Indeed, clockwise rotation of the GW propagation direction was observed using HF Doppler of MSTIDs over the UK (Waldock & Jones, 1986). However, this work found the estimated angle between the TID azimuth ξ to be ~130°–140° clockwise with respect to the wind direction (the propagation direction of TIDs lag the anti-wind direction by 30°–40°). In addition, TIDDBIT observations over Wallops Island, VA, USA also found a clockwise rotation in time with a relative angle between ξ and the background wind direction of ~120°–160° (based on our interpretation of the data shown in Figures 9a and 10a of Crowley and Rodrigues (2012), although they state the relative angle to be ~ 90° in the text). Crowley et al. (1987) observed a counterclockwise rotation of wave azimuth in the southern hemisphere. Importantly, Figures 11f and 11h show that the times when the GWs propagate mostly southward occurs at ~13:30 LST. This is the approximate time (or ~1 hr later) than when the wind from the migrating diurnal tide is northward (Becker, Vadas, et al., 2022). Thus we find a relative angle between ξ and the background wind direction of ~165°–180°. Know that the azimuth of a TID generated by a GW via ion-neutral collisions is the same as the azimuth of this GW for a single ion species ($z > 180$ km) (Nicolls et al., 2014). Therefore, our results agree very well with these previous observations, thus providing a good validation of our method.

Previous studies have shown that GW activity in the lower atmosphere significantly influences the thermosphere/ionosphere during quiet times, including deep convection during the summer (H. Liu et al., 2017; Trinh et al., 2018; Vadas & Liu, 2013; Vadas et al., 2014), and higher-order GWs from wind flow over orography (Becker & Vadas, 2020; Vadas & Becker, 2019) and from the polar vortex in the winter (Becker, Vadas, et al., 2022; Frissell et al., 2016). However, a quantitative understanding of the relative importance of the sources of GWs "from below" is still lacking. To address this, we investigate the monthly changes of the GW amplitudes. In Figure 12, we show the monthly multiplicative mean (μ^*) of the relative density amplitude (Amp.of $\tilde{\rho}$) of GOCE and CHAMP GWs for specific latitude ranges. The first striking observations is that the GW amplitudes at any LST and latitude range show a clear semi-annual variation for both GOCE and CHAMP, being maximum (minimum) at the solstices (equinoxes) in both the northern and southern hemispheres. However, this semi-annual variation is much more important for the GOCE GWs than for the CHAMP GWs, with the solstice maxima being of similar amplitudes. In the CHAMP data, however, the annual variation is much more important, with the JJA maxima being much larger than the DJF maxima for both the northern and southern hemisphere. This difference is presumably due to the dissipation of GWs from molecular viscosity between the different satellite altitudes

of 270 and 370 km, and would occur if the DJF GWs have slower horizontal phase speeds than the JJA GWs (Vadas, 2007).

During 0–12 LST, the GOCE GW intensity is consistently higher at 60°S–60°N (and 0°–60°N) during JJA than at 60°S–60°N (and 60°S–0°) during DJF, with the largest contribution being from 0° to 60°N (blue curve) (see Figure 12a). Thus GWs during 0–12 LST at low- and mid-latitudes are strongest during JJA, which coincides with the peak of the precipitation at 0°–20°N (Cullens et al., 2022). It also coincides with the time of the largest GW peak over the Southern Andes in GW observations near mid-stratospheric (L. Hoffmann et al., 2013) and stratopause (Xu et al., 2023). During 12–24 LST, however, the GWs generally exhibit larger amplitudes during DJF, with the largest contribution being from 0° to 60°N (blue curve) (see Figure 12b). This indicates that the wintertime GWs during 12–24 LST have a stronger impact on the thermosphere than those in the summer thermosphere. For comparison, we also plot the μ* values of GWs for each hemisphere and for the entire globe. As shown in the lower two panels, when GWs in high-latitudes (90°S–60°S and 60°N–90°N) are included, the summer hemisphere consistently exhibits stronger GWs, both for GWs in 0–12 LST (Figure 12c) and 12–24 LST (Figure 12d). This means that the amplitudes of GW events in the polar summer region are generally stronger. The overwhelming numbers of GW occurrence in summer polar region effectively shift μ* values of the whole summer hemisphere higher. Figures 12e and 12f show the monthly variation of the CHAMP GW density amplitudes. The GWs at any LST again are strongest during JJA, which coincides with the peak of the rainfall at 0°–20°N. Cullens et al. (2022) found that the amplitudes of the GWs observed by ICON-MIGHTI at 0°–40°N exhibited semi-annual variation in the mesosphere-lower-thermosphere (MLT), with maximum (minima) at the solstices (equinoxes). That study also showed that the GW zonal wind perturbations, u', at 200 km altitude exhibited mainly an annual variation with a weaker semi-annual variation, with the major (minor) maxima occurring at JJA (DJF) and with the minima occurring at the equinoxes (their Figure 2a). The difference between their results and our GOCE GWs (shown in Figure 12) is that their DJF MIGHTI u' peak is 40% weaker than their JJA peak. This difference likely occurs for the following reason. The dominant sources of the thermospheric GWs during DJF at 0°–40°N (as observed by ICON-MIGHTI) are likely the polar vortex and orographic forcing. Because these GWs would have had to propagate large distances meridionally in order to be observed by MIGHTI at 0°–40°N, most would have had larger meridional than zonal components of their propagation directions, which is equivalent to having larger meridional (than zonal) velocity perturbations. Because Figure 2a in Cullens et al. (2022) only showed u', that figure would have underestimated the total GW amplitude (i.e., $\sqrt{(u')^2+(v')^2}$) during DJF by $\sqrt{2}$ ~1.4, which is a false DJF peak reduction of >30%. Taking this factor into account, our GOCE GW results agree well with the ICON-MIGHTI results.

Overall, the results in GOCE and CHAMP are similar to the results observed by HF Doppler at a similar altitude (Figure 6a of Waldock and Jones (1986), which shows the GW frequency peaks in February and July). We note that the GW amplitudes measured at mid to high latitudes using a meteor radar in the MLT also exhibit a semi-annual variation, with maxima at the solstices (e.g., Figures 11 and 12 of P. Hoffmann et al. (2010)). That behavior is due to the annual variation of the mean wind in the MLT region over mid- and high-latitude regions, which goes through zero (and reverses sign) at the equinoxes (e.g., Figure 4b in R. R. Garcia et al., 1997; P. Hoffmann et al., 2010). When the mean wind is close to zero, the GWs propagating in all directions break and deposit their momentum and energy in the MLT. However, during solstice, those GWs propagating opposite to the mean wind propagate much higher before breaking or dissipating in the thermosphere, thus projecting their semi-annual variation onto the higher-order GWs. Thus, the semi-annual variation observed in Figure 12 here strongly suggest that these GOCE and CHAMP GWs are mainly higher-order GWs from the dissipation of primary GWs from GW sources in the lower/middle atmosphere.

5. Conclusions

In this study, we investigated the thermospheric GWs observed by the GOCE and CHAMP satellites. GWs are essential for providing variability to the thermosphere, generating TIDs, redistributing energy and momentum throughout the Earth's atmosphere, and influencing the dynamics of the thermosphere over a range of spatial and temporal scales. Recent research has shown a strong link between lower atmospheric dynamics, such as polar vortices, and the characteristics of GWs in the thermospheric/ionospheric region.

Although various methods have been employed to study thermospheric GWs, in-situ spacecraft missions equipped with precise accelerometers offer unprecedented accuracy and resolution. Our study leveraged this advantage to determine the intrinsic characteristics of GW events observed as TADs along the satellite tracks. We used a wavelet analysis and the red-noise model to analyze each TAD event and determine if it was a thermospheric GW event. The application of wavelet in this current study was based on 2 assumptions. (a) The spectrum of noise is continuously distributed and can be modeled by the red-noise model. In this simplified model, noise is assumed to have a power (variance) spectral density that decreases as the scale decreases. (b) The GWs that superimposed on the red-noise sequence covers a narrow spectrum instead of a broad dispersive spectrum, so these GWs can be well represented by sinusoidal waves that are superimposed on the red-noise series. Our results showed that those assumptions were generally satisfied but were somewhat conservative for diagnosing TADs in general, because we saw many small-scale TADs that were filtered out when we applied the 95% confidence level as the threshold to extract TADs for our method.

In sum, we analyzed the quiet-time (Kp < 3) TADs from GOCE during November 2009 to October 2013 (at $z \sim 270$ km) and from CHAMP (at $z \sim 370$ km) during 2004–2007. Once we extracted the density and cross-track wind perturbations for the TADs, we used the GW dissipative polarization and dispersion relations, combined with the background thermosphere, to derive the intrinsic properties of some of the GW events (after applying the selection criteria given in Table 1), such as their propagation directions, intrinsic periods, and horizontal wavelengths. Despite the above challenges, our methodology provides valuable insights into the statistical properties of GWs. Here are the findings:

1. We found that ∼17% of TADs in GOCE and 11% of TADs in CHAMP were confidently identified as GW events.
2. The peak horizontal wavelength, intrinsic horizontal phase speed and intrinsic period were λ_H = 585 km, c_{IH} = 688 m/s and τ_{Ir} = 14.3 min for the GOCE GWs and λ_H = 655 km, c_{IH} = 768 m/s and τ_{Ir} = 14.4 min for the CHAMP GWs, respectively. The increase of c_{IH} with height is consistent with GW dissipation from molecular viscosity. Such fast phase speeds show that most of these GWs were generated in the thermosphere, not in the lower/middle atmosphere (for which it is necessary that those GWs have c_{IH}<0.9*310 m/s∼ 280 m/s).
3. We also find a second population of GOCE GWs with λ_H = 100–400 km, c_{IH} = 50–250 m/s and τ_{Ir} = 10–50 min. These slower GWs were also present in CHAMP but much less frequently. It is possible that many of these second-populations GW were from the lower/middle atmosphere.

Next, we provided global morphology maps of the thermospheric GWs (instead of global TAD maps) from GOCE and CHAMP for the first time. The findings derived from these maps are:

1. High latitudes consistently exhibit higher GW intensities, with polar summer regions showing the strongest GW amplitudes. Although a significant amount of the polar GWs in thermosphere may be higher-order GWs from lower/middle atmospheric processes (such as orographic forcing, the polar vortex, and deep convection), some of our diagnosed GWs may also be generated by Joule heating, even though we attempted to minimize these latter GWs by restricting $Kp < 3$ for allowed events.
2. We also found that higher-order GW hotspots occurred during the winter thermosphere at mid to high latitudes, likely from primary GWs from orographic forcing and the polar vortex. We found that the GOCE GW amplitudes exhibited semi-annual variations, with maxima in January and July, and minima at the equinoxes. In contrast, the CHAMP GW amplitudes exhibited mainly annual variation (with a weaker semi-annual variation), with the major (minor) maximum in July (January), and with minima at the equinoxes. These seasonal variations show that a significant fraction of the GOCE and CHAMP GWs (identifiable by our method) are likely not from Joule heating, but are higher-order GWs originating from the dissipation of primary GWs generated in the lower/middle atmosphere. This dissipation is shaped by seasonally varying background winds during GW propagation and primary GW sources.

Finally, we found that the average propagation direction of the CHAMP GWs exhibited a clear diurnal cycle, with clockwise (counter-clockwise) occurring for GWs in the northern (southern) hemisphere, in agreement with previous observations of TIDs. In addition, we found that the CHAMP GWs had equatorward propagation occurring at ∼13:00 LST. This suggests that the predominant propagation direction of CHAMP GWs is approximately opposite to the background wind direction.

Our novel approach holds significant potential for studying GWs *in-situ* observed by other LEO satellite missions, expanding our understanding of thermospheric GWs at different altitudes and improving our prediction of TIDs generated by those GWs. The paper provides insights that underscore the complex interplay of GWs from different sources during different seasons, as well as the LST-dependent and latitudinal variations created by these GWs. This research lays the groundwork for future studies on GWs using in-situ measurements from various satellite missions such as GDC, enhancing our knowledge of these important atmospheric phenomena.

Appendix A: Symbolic Conventions (Abbreviations, Acronyms, and Symbols)

Quantity	Meaning	Note
ρ	Extrapolated density at a fixed altitude (e.g., 270 km for GOCE), derived from in-situ measurements and extrapolated according to exponential-fitted density scale height of one orbit of observations.	Unit: kg/m^3
u_{xtrack}	Cross-track wind in one orbit of observations.	Unit: m/s
W, W_{mod}	Wavelet spectrum; modified (not to be confused with "modulus") wavelet spectrum.	Defined in Section 3.1 and Appendix B.
$\overline{\$}$, $\$'$	$\overline{\$}$: Mean of variable $.$\$'$: Deviations due to perturbations and noise.	$\$' = \$ - \overline{\$}$
$\tilde{\rho}$	Reconstruction of $\rho'/\overline{\rho}$ with confidence >95% and $\lambda_{\text{track}} < 3{,}000$ km.	Unit: %
$\tilde{u}_{\text{xtrack}}$	Reconstruction of u'_{xtrack} with confidence >95% and $\lambda_{\text{track}} < 3{,}000$ km.	Unit: m/s
ψ, ξ, ϕ	ψ: Azimuth of satellite track.ξ: Azimuth of GW propagation direction.ϕ: difference between 2 azimuths.	$\phi = \psi - \xi$
ω_I	Complex intrinsic frequency.	$\omega_I = \omega_{\text{Ir}} + i\omega_{\text{Ii}}$
τ_{Ir}	Intrinsic period of GW.	$\tau_{\text{Ir}} = 2\pi/\omega_{\text{Ir}}$
λ_H; λ_z	Horizontal and vertical wavelength of a GW.	
λ_{track}	Wavelength of a GW along in-situ observation track (directly derived from wavelet analysis).	λ_{track} is derived directly from wavelet analysis
λ_ψ	The instantaneous wavelength of a GW along satellite path (with azimuth ψ).	$\lambda_\psi = \lambda_H / \lvert\cos\phi\rvert$
$\Delta\lambda$	Difference between λ_ψ and λ_{track} due to the movement of the satellite.	$\Delta\lambda = \lvert\lambda_{\text{track}} - \lambda_\psi\rvert$
k, l, m; k_H	k,l,m are the zonal, meridional, and vertical wave numbers, respectively.k_H is the horizontal wave number.	$(k,l,m) = \frac{2\pi}{\left(\frac{\lambda_H}{\sin\xi}, \frac{\lambda_H}{\cos\xi}, \lambda_z\right)}$;$k_H = \sqrt{k^2 + l^2} = 2\pi/\lambda_H$
$\boldsymbol{U}$; $\overline{U}, \overline{V}$; U_H; azi$_U$	$\boldsymbol{U}$: vector that represents the background wind.$\overline{U}, \overline{V}$: Zonal and meridional components of the background wind.U_H: Background horizontal wind along the direction of GW propagation. azi$_U$: azimuth of horizontal direction of $\boldsymbol{U}$.	$\boldsymbol{U} = \left(\overline{U}, \overline{V}\right)$;$U_H = \left(k\overline{U} + l\overline{V}\right)/k_H$ or $U_H = \lvert\boldsymbol{U}\rvert\cos(\xi - \text{azi}_U)$
v_{sat}	Ground-based satellite velocity.	
c_{IH}; c_H	c_{IH}: intrinsic horizontal phase speed of a GW.c_H: ground-based horizontal phase speed of a GW.	$c_{\text{IH}} = \frac{\lambda_H}{\tau_{Ir}}$;$c_H = c_{\text{IH}} + U_H$
$\hat{\$}$	Fourier Transform of a variable $.	
$\lvert\$\rvert$	Modulus (if $ is a complex number, array, or function) or magnitude of a variable $.	
arg($) *or* $_{\text{arg}}$	Argument of a complex number, array, or function $.	
$\Re\{\$\}$ and $\Im\{\$\}$	Real and imaginary part of a complex number, array, or function $.	

Appendix B: Deriving the Unbiased Wavelet Spectrum $W_{mod}(n, s)$ and Determine the Corresponding Uncertainties.

According to Torrence and Compo (1998, hereafter TC98), for a discrete signal sequence x_n, the *discrete Fourier transform* (DFT) of x_n is

$$\hat{x}_k = \frac{1}{N}\sum_{n=0}^{N-1} x_n e^{-\frac{2\pi i k n}{N}}, \tag{B1}$$

where $n = 0\ldots N-1$ is the index of x_n and $k = 0\ldots N-1$ is the frequency index. In practice, x_n usually represents a time series (e.g., in TC98), and each increment in n corresponds to the time step δt. However in the current study, x_n represents a series along the satellite track with length step δx (which is the ground-based distance that satellite travels in 10 s). The operator (^) denotes the Fourier Transform. The *complex wavelet spectrum* $W(n, s)$ is defined by the convolution theorem:

$$W(n, s) = \sum_{k=0}^{N-1} \hat{x}_k \hat{\psi}^*(s\omega_k) e^{\frac{2\pi i k n}{N}}, \tag{B2}$$

where ω_k is the angular frequency defined by $\omega_k = \mathrm{sgn}(N/2 - k)(2\pi k/N\delta x)$. The wavelet function $\hat{\psi}(s\omega_k)$ is given by Equation 6 in TC98. We designate the Morlet wavelet defined in their Table 1 to be wavelet base function $\hat{\psi}_0$. The (*) indicates the complex conjugate. Following Section 3f in TC98, the *wavelet scale s* is written as fractional powers of two and in the unit of the spatial resolution δx along the satellite track:

$$s = s_j = s_0 2^{j\delta j} (j = 0, 1, \ldots, J), \tag{B3}$$

where s_0 is the smallest resolvable scale. In this study, we use $\delta j = 0.25$ and $s_0 = 2\delta x$ for this paper. J determines the largest scale of s_j within the length of the input series x_n.

One of our assumptions is that when no TAD signal is present in the GOCE or CHAMP data sets, both the variations in the density and cross-track wind along the orbit can be modeled by red noise. Following TC98, a simple model for red noise is the univariate lag−1 autoregressive [AR(1), or Markov] process:

$$x_n = \alpha x_{n-1} + z_n, \tag{B4}$$

where α is the assumed lag-1 autocorrelation, $x_0 = 0$, and z_n is Gaussian white noise. Following Gilman et al. (1963), the discrete Fourier power spectrum at frequency index k (here $k = 0\ldots N/2$), after normalizing with the factor $1/\sigma^2$ (where σ^2 is the variance of x_n), is:

$$P_k = \frac{1 - \alpha^2}{1 + \alpha^2 - 2\alpha\cos(2\pi k/N)}. \tag{B5}$$

The meaning of Equation B5 is: noise has a power spectral density that decreases as the scale decreases. Since each $\hat{x}_k$ at a fixed k is normally distributed in the red noise model, then the wavelet coefficients (the band-passed inverse Fourier components) should also be normally distributed (TC98). Therefore, when the wave signal is absent or subtracted from the series x_n, $W(n, s)$ is normally distributed in the complex plane at (n, s), and the *wavelet power spectrum* $|W(n, s)|^2$ of red noise is chi-square distributed:

$$\Re\{W(n,s)\} \text{ and } \Im\{W(n,s)\} \Rightarrow \mathcal{N}\left(0, \frac{1}{2}\sigma^2 P_k\right), \quad |W(n,s)|^2 \Rightarrow \frac{1}{2}\sigma^2 P_k \chi_2^2 \tag{B6}$$

where χ_2^2 is the chi-square distribution with two degrees of freedom. According to the chi-square distribution table, the probability $P\left\{\chi_2^2 > \chi_{2,a=0.05}^2\right\} = 0.05$, we have $\chi_{2,a=0.05}^2 \approx 5.992$. It means that if there is a peak in the wavelet power spectrum that is higher than $\frac{1}{2}\sigma^2 P_k \chi_{2,a=0.05}^2$, we say that it is a real wave signal (instead of noise) in the observations with confidence higher than 95%, because the probability of this peak to be noise is less than 5%.

As shown by the in Maraun and Kurths (2004, see their Figure 2) and pointed out by Y. Liu et al. (2007), the wavelet power spectrum $W(n, s)$ calculated by TC98's method is good when the input is dominated by stochastic (noisy) processes, but has a bias toward larger scales s when the noise input is superposed by monochromatic

waves. To reduce this bias, Chen (2016, hereafter C16) replaced the wavelet function $\hat{\psi}(s\omega_k)$ in TC98 by a modified wavelet function $\hat{\psi}_{\mathrm{mod}}(s\omega_k)$. The conversion between them is

$$\hat{\psi}_{\mathrm{mod}}(s\omega_k) = C_F(s)\hat{\psi}(s\omega_k)\left[\text{correction factor } C_F(s) = \left(\frac{\delta t}{2\pi^{\frac{1}{2}} s}\right)^{\frac{1}{2}}\right]. \tag{B7}$$

Following C16, we derive the *unbiased wavelet spectrum* $W_{\mathrm{mod}}(n, s)$ using $\hat{\psi}_{\mathrm{mod}}(s\omega_k)$ when we assume the input has no noise:

$$W_{\mathrm{mod}}(n, s) = 2\sum_{k=0}^{N-1} \hat{x}_k \hat{\psi}^*_{\mathrm{mod}}(s\omega_k) e^{\frac{2\pi i k n}{N}} = 2\sum_{k=0}^{N-1} \hat{x}_k C_F \hat{\psi}(s\omega_k) e^{\frac{2\pi i k n}{N}} = 2C_F W(n, s). \tag{B8}$$

When x_n consists of monochromatic waves, $W_{\mathrm{mod}}(n, s)$ is equivalent to the FFT. Since the size of the frequency domain of $W_{\mathrm{mod}}(n, s)$ $(k = 0 \ldots N/2)$ is one-half of FFT of x_n $(k = 0 \ldots N - 1)$, the factor of two in the right-hand side of the equation is needed to derive the correct amplitudes. Therefore, if uncertainties are included, the corresponding expectation of the amplitude and phase at (n, s) is defined as:

$$\begin{cases} E[|W_{\mathrm{mod}}|] = 2C_F\sqrt{\Re\{W(n,s)\}^2 + \Im\{W(n,s)\}^2} \\ E\left[\arg(W_{\mathrm{mod}})\right] = \operatorname{atan}2(\Im\{W(n,s)\}, \Re\{W(n,s)\}) \end{cases}. \tag{B9}$$

Since the complex wavelet spectrum $W(n, s)$ is expected to have a 2D normal distribution in the complex plane given by Equation B5, the expected uncertainty (conventionally referred to as "half-length of error bar") in amplitude can be quantified by the standard deviation of either $\Re\{W_{\mathrm{mod}}(n, s)\}$ or $\Im\{W_{\mathrm{mod}}(n, s)\}$, which is

$$\mathrm{SD}_{\mathrm{Amp}}(n, s) = \frac{\sqrt{2}\sigma\sqrt{P_k}}{2}. \tag{B10}$$

For TADs with high peaks in amplitude spectrum (i.e., when $\mathrm{Amp}_n(s) \gg \mathrm{SD}_{\mathrm{Amp}}(n, s)$, which brings high confidence to say it is not noise), the corresponding uncertainty in phase can be represented by

$$\mathrm{SD}_{\mathrm{Pha}}(n, s) = \frac{\sqrt{2}\sigma\sqrt{P_k}}{2|W_{\mathrm{mod}}(n, s)|}. \tag{B11}$$

Note that the counterpart of the "equivalent Fourier period" in TC98 is the along track wavelength (λ_{track}) in our study, and thus gives a value of $\lambda_{\mathrm{track}} = 1.03$s for the Morlet wavelet for the *nondimensional frequency* $\omega_0 = 6$. Therefore, variables that can be written as functions of (n, s) can be written as functions of $(n, \lambda_{\mathrm{track}})$ as well. Based on the expectation of W_{mod} defined by Equation B9, the distribution of W_{mod} in the complex plane is:

$$\begin{cases} \Re\{W_{\mathrm{mod}}(n,s)\} \Rightarrow \mathcal{N}\left(E[|W_{\mathrm{mod}}|] * \cos\left(E\left[\arg(W_{\mathrm{mod}})\right]\right), \frac{1}{2}\sigma^2 P_k\right) \\ \Im\{W_{\mathrm{mod}}(n,s)\} \Rightarrow \mathcal{N}\left(E[|W_{\mathrm{mod}}|] * \sin\left(E\left[\arg(W_{\mathrm{mod}})\right]\right), \frac{1}{2}\sigma^2 P_k\right) \end{cases} \tag{B12}$$

Appendix C: Deriving the PS and AR of Perturbations of $\hat{\rho}$ and $\hat{u}_{xtrack}$ Along the Satellite Track Direction (ψ) as Functions of ϕ and λ_z

Following Vadas et al. (2019), the complex, dispersion relation for acoustic waves and GWs damped by molecular viscosity and thermal diffusivity is a function of wave number vectors $k_H = (k, l)$ and m and the complex intrinsic frequency ω_I:

$$(\omega_I - i\alpha\nu)\left(\omega_I - \frac{i\alpha\nu}{\mathrm{Pr}}\right)\left(\boldsymbol{k}^2 + \frac{1}{4\mathcal{H}^2}\right) - \left[k_H^2 N_B^2 + \frac{\omega_I}{c_s^2}\left(\omega_I - \frac{i\gamma\alpha\nu}{\mathrm{Pr}}\right)(\omega_I - i\alpha\nu)\left(\omega_I - i\alpha\nu\left(1 + \frac{\mathrm{a}}{3}\right)\right)\right] = 0. \tag{C1}$$

The compressible dissipative GW complex polarization relations for the density and horizontal wind perturbations (substituting $\hat{u}_H \to \tilde{u}_H$, $\hat{w} \to \tilde{w}$, $\hat{\rho} \to \tilde{\rho}$ into Equations 11 and 13 of Vadas et al. (2019), since the operator ^ has already been used to denote the Fourier Transform in this paper) along GW propagation direction ξ can be expressed as two equations:

$$\frac{\tilde{\rho}}{\tilde{w}} = \frac{1}{{c_s}^2 D}\left[\gamma\left(i\omega_I + \frac{\gamma\alpha\nu}{Pr}\right)\left(i\omega_I + \nu\left(\alpha + \frac{a}{3\mathcal{H}}\left(im + \frac{1}{2\mathcal{H}}\right)\right)\right) - \frac{(\gamma-1){c_s}^2}{\mathcal{H}}\left(im - \frac{1}{2\mathcal{H}}\right)\right] \tag{C2}$$

$$\frac{\tilde{u}_H}{\tilde{w}} = \frac{\gamma}{ik_H {c_s}^2 D}\left[i\omega_I\left(i\omega_I + \frac{\gamma\alpha\nu}{Pr}\right)\left(i\omega_I + \nu\left(\alpha + \frac{a}{3}\left(\alpha + {k_H}^2\right)\right)\right) + {c_s}^2\left(m^2 + \frac{1}{4\mathcal{H}^2}\right)\left(i\omega_I + \frac{\alpha\nu}{Pr}\right)\right] \tag{C3}$$

Respectively. Here $\boldsymbol{k} = (k, l, m) = 2\pi/(\lambda_x, \lambda_y, \lambda_z)$ is the full wave vector. The background characteristics in equations (C1)–(C3), such as N_B (buoyancy frequency), c_s (sound speed), $\mathcal{H}$ (density scale height), ν (kinematic viscosity, $\nu = \mu/\overline{\rho}$, μ is the molecular viscosity), γ (ratio of specific heats, $\gamma = c_p/c_v$, in which c_p and c_v are isobaric and isochoric specific heat respectively), etc., are determined directly or indirectly by gravity and background density using the NRLMSIS2.1 model, while α and D are functions of these characteristics and k_H and m. Finally, a in Equations C1–C3 is set to be 1 to include the bulk viscosity in addition to the shear viscosity in the viscous stress tensor. Please refer to Section 4.3 in Vadas et al. (2019) for further information.

By dividing Equations C2 and C3, the vertical wind perturbation $\tilde{w}$ on the left-hand-sides (LHSs) of Equations C2 and C3 cancel out. The ratio of the right-hand-sides (RHSs) of Equations C2 and C3 is still a function of λ_H and λ_z. Therefore, the ratio of RHSs of Equations C2 and C3 can be expressed as functions of the horizontal and vertical wavelengths. We use F to denote this function:

$$\frac{\tilde{\rho}}{\tilde{u}_H} = \frac{\text{Equation (C2)}}{\text{Equation (C3)}} = F(\lambda_H, -\lambda_z). \tag{C4}$$

Since the two perturbations $\tilde{\rho}$ and $\tilde{u}_H$ are expressed as complex numbers, the LHS of (C4) is also a complex number. Its argument (i.e., $\arg(\tilde{\rho}/\tilde{u}_H)$) is equal to the PS between $\tilde{\rho}$ and $\tilde{u}_H$ but with an opposite sign. Its modulus (i.e., $|\tilde{\rho}/\tilde{u}_H|$) is equal to the AR of $\tilde{\rho}$ and $\tilde{u}_H$. Here we use the subscript ξ to denote the GW propagation direction. Then the PS and AR of $\tilde{\rho}$ and $\tilde{u}_H$ along GW propagation direction ξ are:

$$\begin{cases} \mathrm{PS}_\xi(\tilde{\rho}, \tilde{u}_H) = -\arg(F(\lambda_H, -\lambda_z)) = -\arg\left(\frac{\tilde{\rho}}{\tilde{u}_H}\right) \\ \mathrm{AR}(\tilde{\rho}, \tilde{u}_H) = |F(\lambda_H, -\lambda_z)| = |\frac{\tilde{\rho}}{\tilde{u}_H}| \end{cases}. \tag{C5}$$

Figure 2 visualizes $\mathrm{PS}_\xi(\tilde{\rho}, \tilde{u}_H)$ and $\mathrm{AR}(\tilde{\rho}, \tilde{u}_H)$ at a specific time (UTC 2010-07-05 22:53:00) and specific location (79.43°S, 75.53°E, z = 270 km) during the quiet-time austral winter (Kp index = 1−).

To derive the PS and AR between two perturbation variables of a GW along the satellite track azimuth ψ based on (C5), the value of ϕ should be taken into consideration. When $\phi \in (-0.5\pi, 0.5\pi)$, the PS of $\hat{\rho}$ and $\hat{u}_H$ along the satellite direction ψ is equal to $\mathrm{PS}_\xi(\tilde{\rho}, \tilde{u}_H)$, otherwise they have the opposite sign. Thus we have

$$\mathrm{PS}_\psi(\tilde{\rho}, \tilde{u}_H) = \mathrm{sgn}(\cos\,\phi) * \mathrm{PS}_\xi(\tilde{\rho}, \tilde{u}_H). \tag{C6}$$

Because $\tilde{u}_{\mathrm{xtrack}} = -\tilde{u}_H * \sin\,\phi$ (as shown in Figure 3), we get

$$PS_\psi(\tilde{u}_H, \tilde{u}_{\mathrm{xtrack}}) = \begin{cases} \pi\,(\sin\,\phi > 0) \\ 0\,(\sin\,\phi < 0) \end{cases} = 0.5(1 + \mathrm{sgn}(\sin\,\phi))\pi. \tag{C7}$$

Therefore, we get the equation for PS between $\hat{\rho}$ and $\hat{u}_{xtrack}$ of a GW along satellite track azimuth ψ:

$$\mathrm{PS}_{\psi}(\tilde{\rho},\tilde{u}_{\mathrm{xtrack}}) = PS_{\psi}(\tilde{\rho},\tilde{u}_{H}) + \mathrm{PS}_{\psi}(\tilde{u}_{H},\tilde{u}_{\mathrm{xtrack}}) = \mathrm{sgn}(\cos\phi) * \mathrm{PS}_{\xi}(\tilde{\rho},\tilde{u}_{H}) + 0.5(1+\mathrm{sgn}(\sin\phi))\pi. \quad \text{(C8)}$$

Deriving AR of $\hat{\rho}$ and $\hat{u}_H$ of a GW along satellite track azimuth ψ is much easier. Because $\tilde{u}_{\mathrm{xtrack}} = -\tilde{u}_H * \sin\phi$, we have $\mathrm{AR}_{\psi}(\tilde{u}_H,\tilde{u}_{\mathrm{xtrack}}) = |\sin\phi|^{-1}$, so

$$\mathrm{AR}_{\psi}(\tilde{\rho},\tilde{u}_{\mathrm{xtrack}}) = \mathrm{AR}(\tilde{\rho},\tilde{u}_{H}) * \mathrm{AR}_{\psi}(\tilde{u}_{H},\tilde{u}_{\mathrm{xtrack}}) = \frac{\mathrm{AR}(\tilde{\rho},\tilde{u}_{H})}{|\sin\phi|}. \quad \text{(C9)}$$

Analogous to Equations C4 and C5, suppose the observed perturbation ratio $\tilde{\rho}/\tilde{u}_{xtrack}$ along satellite direction ψ can be written as a function of G:

$$\frac{\tilde{\rho}}{\tilde{u}_{\mathrm{xtrack}}} = G(\lambda_H, -\lambda_z, \phi), \quad \text{(C10)}$$

and PS and AR of $\tilde{\rho}$ and $\tilde{u}_{\mathrm{xtrack}}$ of a GW along direction ψ can be written as functions $-\arg(G)$ and $|G|$, as derived in Equations C8 and C9, we have

$$\begin{cases} PS_{\psi}(\tilde{\rho},\tilde{u}_{\mathrm{xtrack}}) = -\arg(G) = \mathrm{sgn}(\cos\phi) * (-F_{arg}) + 0.5(1+\mathrm{sgn}(\sin\phi))\pi \\ AR_{\psi}(\tilde{\rho},\tilde{u}_{\mathrm{xtrack}}) = |G| = \frac{|F|}{|\sin\phi|} \end{cases}. \quad \text{(C11)}$$

Although G in Equation C10 is a function of three independent variables (λ_H, $-\lambda_z$, ϕ), λ_H is dependent on ϕ. (The function λ_H with respect to ϕ, i.e., $k_H = 2\pi/\lambda_H = H(\phi, -\lambda_z)$, is derived in Appendix D. See the derivation of Equation D7) Therefore, G can be reduced to a function of two unknown independent variables that Equation C10 can be written as $(\tilde{\rho}/\tilde{u}_{\mathrm{xtrack}}) = G(\phi, -\lambda_z)$. Since the modules and argument of its LHS $(\tilde{\rho}/\tilde{u}_{\mathrm{xtrack}})$ can be extracted from amplitude and phase spectra using unbiased wavelet analysis, the two unknowns $(\phi, -\lambda_z)$ can be solved by using charts of PS_{ψ} and AR_{ψ} as "look up tables". The other GW intrinsic parameters, such as, λ_H, τ_{Ir}, ξ, etc., can be derived directly based on $(\phi, -\lambda_z)$ solutions.

Appendix D: Derivation of λ_H of a GW as a Function of ϕ, Background Wind, and Satellite Movement Parameters.

As shown in Figure D1, the distance between the phase lines of the GW perturbations along the direction of azimuth ψ at a fixed time t is λ_{ψ}. The along-track wavelength of the GW perturbations observed by the satellite is λ_{track}. If we assume the satellite velocity v_{sat} is much larger than the ground based horizontal phase speed of a GW, then the observed wavelength along track λ_{track} is very close to λ_{ψ} (i.e., when $v_{\mathrm{sat}} \to \infty$, $\lambda_{\mathrm{track}} \to \lambda_{\psi}$). This assumption may not be reasonable in extreme scenarios, especially when $|\cos\phi|$ is small so the satellite velocity along the GW propagation direction $|v_{\mathrm{sat}}\cos\phi|$ and the GW horizontal phase speed c_H are comparable. Therefore, it is necessary to determine λ_{ψ} as a function of λ_{track} for the extracted measurements before solving for the GW intrinsic parameters.

As shown in Figure D1, $\Delta\lambda$ denotes the difference between λ_{track} and λ_{ψ},

$$\Delta\lambda = \begin{cases} \lambda_{\mathrm{track}} - \lambda_{\psi} \left(\text{when} -\frac{\pi}{2} < \phi < \frac{\pi}{2}\right) \\ \lambda_{\psi} - \lambda_{\mathrm{track}} \left(\text{when} \frac{\pi}{2} < \phi < \frac{3\pi}{2}\right) \end{cases}, \quad \text{(D1)}$$

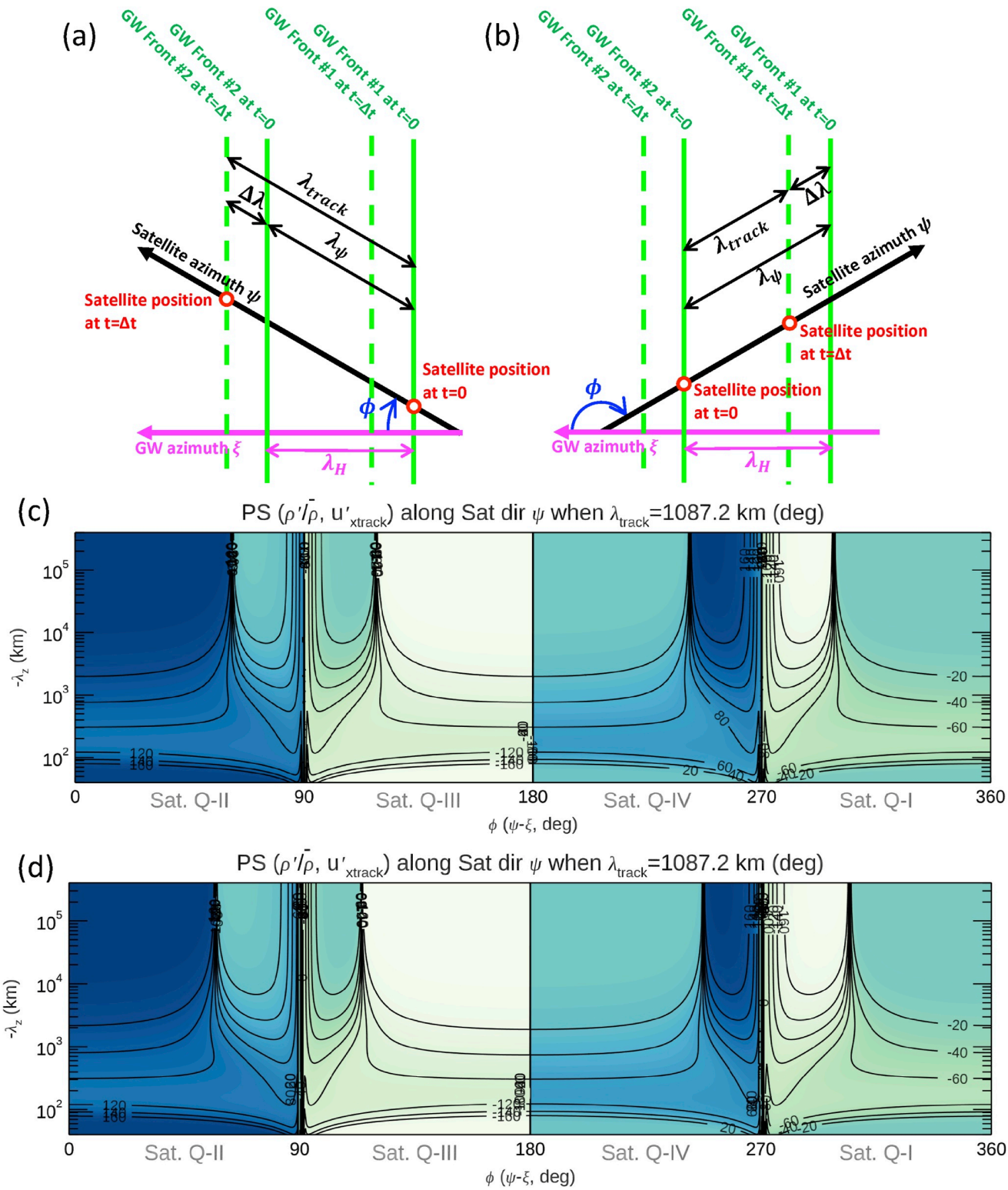

Figure D1. (a) Illustration of sampling effect when ϕ is in the range of $(-0.5\pi, 0.5\pi)$, corresponding to scenario when the satellite overtakes the GWs; (b) The same as (a) but when ϕ is in the range of $(0.5\pi, 1.5\pi)$, corresponding to scenario when the satellite meets the gravity waves. (c) Diagram of function $\mathrm{PS}(\tilde{\rho}, \tilde{u}_{\mathrm{xtrack}}) = -G_{\mathrm{arg}}(\phi, -\lambda_z)$ without considering sampling effect by assuming v_{sat} = infinite for GOCE satellite; (d) The same as (c) but considering sampling effect with v_{sat} = 7,765 m/s for GOCE satellite.

Suppose the satellite and the first GW wavefront #1 meet at initial moment $t = 0$ and then the satellite and the next GW wavefront #2 meet at moment $t = \Delta t$, we get

$$\Delta t = \begin{cases} \frac{\lambda_H}{v_{\text{sat}} \cos \phi - c_H} \left(\text{when } -\frac{\pi}{2} < \phi < \frac{\pi}{2} \right) \\ \frac{\lambda_H}{v_{\text{sat}}(-\cos \phi) + c_H} \left(\text{when } \frac{\pi}{2} < \phi < \frac{3\pi}{2} \right) \end{cases}. \tag{D2}$$

On the RHS, the numerator is the distance between the satellite and wavefront #2 at the initial moment, while the denominator is their speed difference (when $\phi \in (-0.5\pi, 0.5\pi)$) or speed sum (when $\phi \in (0.5\pi, 1.5\pi)$) along the GW propagation direction. Therefore, we have

$$\Delta\lambda |\cos \phi| = c_H \Delta t = \begin{cases} \frac{c_H \lambda_H}{v_{\text{sat}} \cos \phi - c_H} \left(\text{when } -\frac{\pi}{2} < \phi < \frac{\pi}{2} \right) \\ \frac{c_H \lambda_H}{v_{\text{sat}}(-\cos \phi) + c_H} \left(\text{when } \frac{\pi}{2} < \phi < \frac{3\pi}{2} \right) \end{cases} \tag{D3}$$

Combining Equations D1 and D3 we have

$$\lambda_{track} - \lambda_\psi = \frac{c_H \lambda_H / |\cos \phi|}{v_{sat} \cos \phi - c_H} = \frac{c_H \lambda_\psi}{v_{sat} \cos \phi - c_H}. \tag{D4}$$

According to the definition of the horizontal phase speed c_H in Appendix A, we have:

$$c_H = \frac{\lambda_H}{\tau_{Ir}} + U_H = \frac{\lambda_\psi |\cos \phi|}{\tau_{Ir}} + U_H. \tag{D5}$$

Plugging Equation D5 into Equation D4 and solving for λ_ψ we get the solution:

$$\lambda_\psi = \frac{(v_{\text{sat}} \cos \phi - U_H)\lambda_{\text{track}} \tau_{\text{Ir}}}{\lambda_{\text{track}} |\cos \phi| + v_{\text{sat}} \tau_{\text{Ir}} \cos \phi}. \tag{D6}$$

Since $\lambda_H = \lambda_\psi * |\cos\phi|$ we get

$$\lambda_H = \frac{(v_{\text{sat}} \cos \phi - U_H)\lambda_{\text{track}} \tau_{Ir}}{\lambda_{\text{track}} + v_{\text{sat}} \tau_{\text{Ir}} * \text{sgn}(\cos \phi)} \tag{D7}$$

or

$$k_H = \frac{\lambda_{\text{track}} \omega_{Ir} + 2\pi * v_{\text{sat}} * \text{sgn}(\cos \phi)}{\lambda_{\text{track}}(v_{\text{sat}} \cos \phi - U_H)}. \tag{D8}$$

As shown by Equation D7, the horizontal wavelength λ_H of a GW can be expressed as a function with respect to 5 variables: ϕ, τ_{Ir}, λ_{track}, v_{sat} and U_H (a function of full background wind $\boldsymbol{U}$ and ϕ). Although τ_{Ir} or ω_{Ir} is a function of the wavenumbers k_H and m based on the complex, dispersion relation for GWs, by substituting k_H in Equation C1 with Equation D8, the dissipative dispersion relation becomes a function for ω_I of dependent variables ϕ and λ_z. Therefore, ω_I at a given (ϕ, $-\lambda_z$) can be solved using Newton's method, and Equation D8 is referred to as a function $k_H = 2\pi/(\lambda_\psi * |\cos\phi|) = H(\phi, -\lambda_z, \lambda_{\text{track}}, v_{\text{sat}}, \boldsymbol{U})$. Since λ_{track} is determined by each peak in the wavelet spectrum, the satellite velocity v_{sat} is obtained from the GOCE and CHAMP data set, and the background wind vector $\boldsymbol{U}$ is obtained from the HWM14 model, there are only two essential unknowns (ϕ and $-\lambda_z$) for solving Equation D7 or function H. By plugging function $k_H = H(\phi, -\lambda_z)$ into the complex function F (Equation 1), we derive complex function G (Equation 4 or Equation C11).

The lower two panels in Figure D1 shows the different results for function $-G_{\text{arg}}(\phi, -\lambda_z)$ without considering the Doppler shift (Figure D1c, where v_{sat} = infinite) and with considering the Doppler shift (Figure D1d, where v_{sat} = 7,765 m/s is GOCE's velocity) due to sampling effect in satellite's movement. Note that in Figure D1c, the shape of the contours in the four quadrants perfectly mirror each other around the boundaries of quadrant, but in Figure D1c the contours are slightly shifted because of considering the sampling effect. Therefore, the sampling effect due to a satellite's movement is very small but still noticeable.

Appendix E: Flowchart of Data Processing.

Flowchart in Figure E1 visualizes the whole procedure to extract TADs (left half of the figure) and identify GWs from TAD events (right half of the figure).

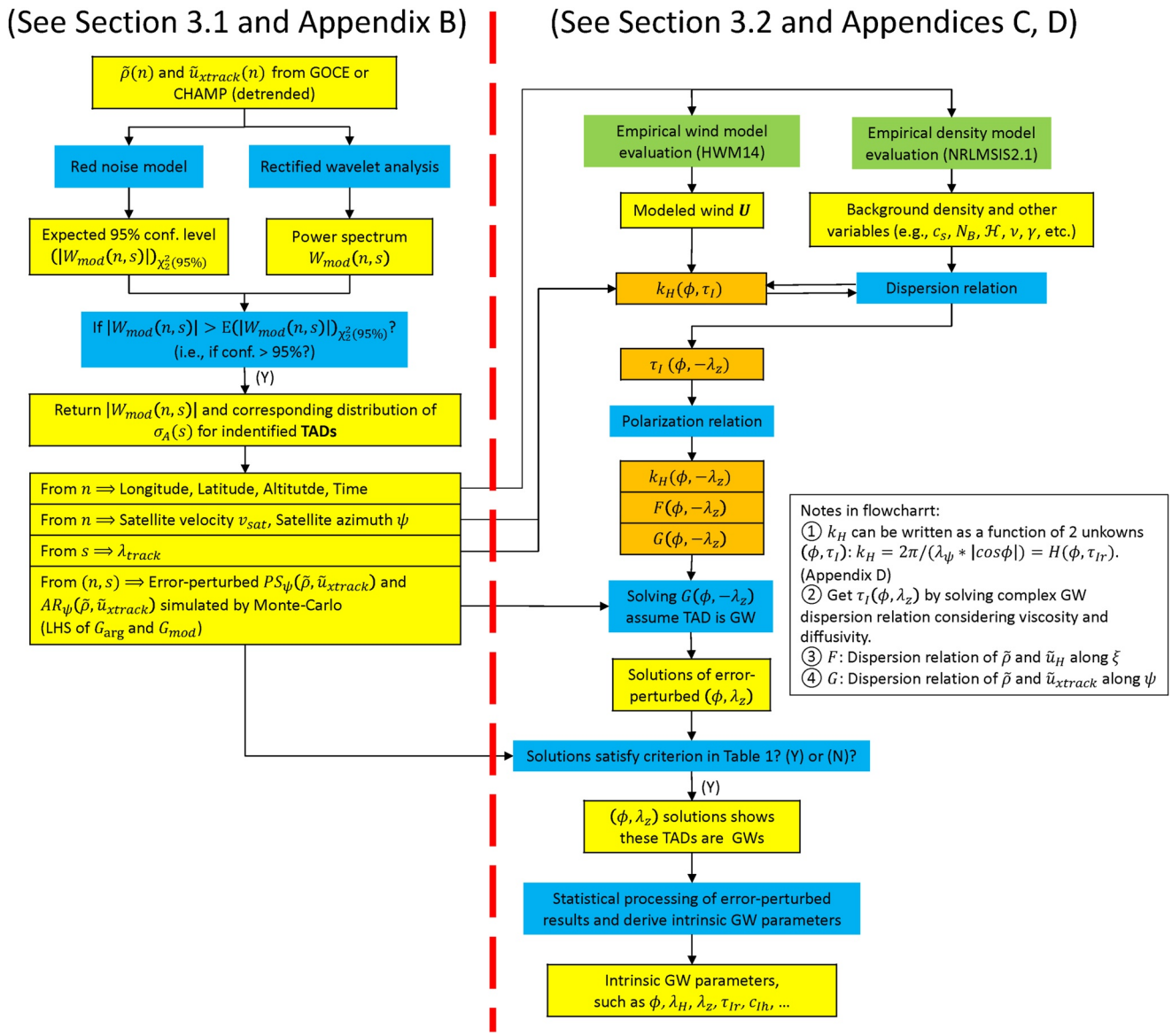

Figure E1. The whole procedure to extract traveling atmospheric disturbances (TADs) (left half of the chart) and identify gravity waves from TAD events (right half of the chart). Meaning of box with different colors: yellow = data sets, blue = processing modules, green = models, orange = functions or parameter spaces.

Appendix F: The Characteristics of GWs Generated by Tohoku-Oki Earthquake/Tsunami.

R. F. Garcia et al. (2014) derived the characteristics of GWs excited by the Tohoku-Oki Earthquake/Tsunami at 05:46 UTC on 11 March 2011. Here we apply our method to the GWs in the same case. In Figure F1, we show the intrinsic parameters of the GWs derived using our method for the GWs from 3 consecutive GOCE tracks following the Earthquake/Tsunami. We find that all GWs are propagating away from the source, as expected.

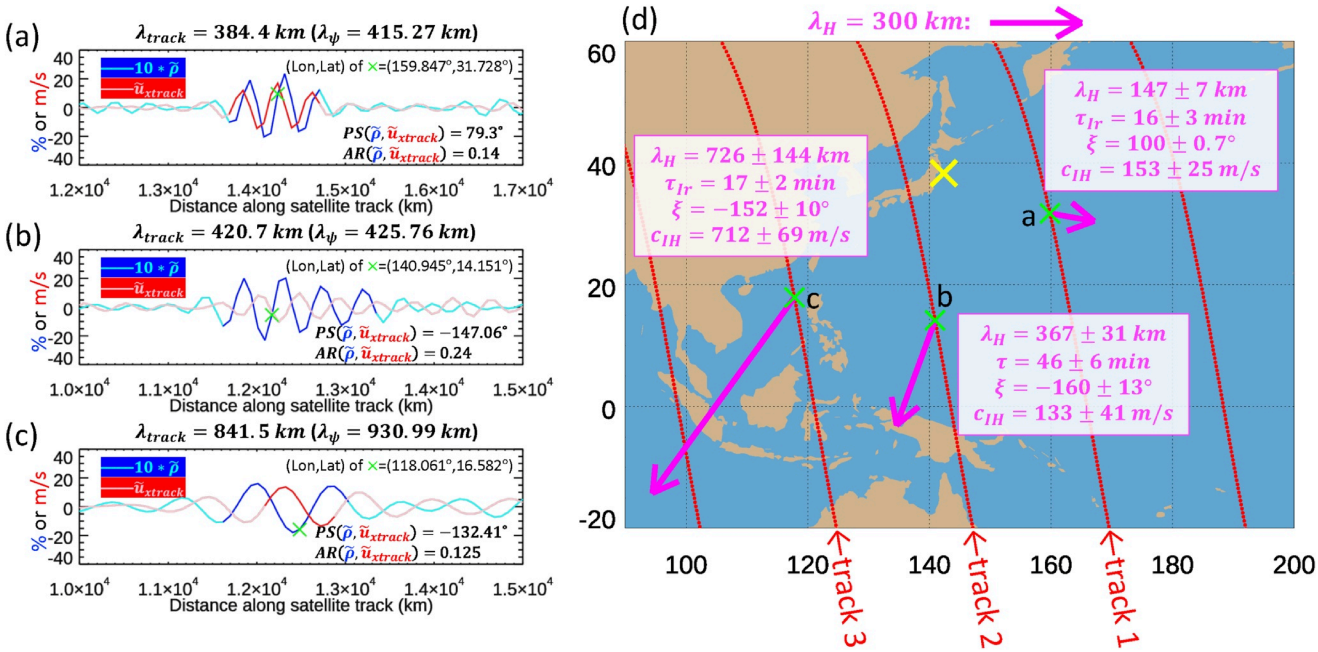

Figure F1. Methodology application using the GOCE gravity wave (GW) cases generated by Tohoku-Oki earthquake at 05:46 UTC on 11 March 2011. (a) The reconstructed perturbation pair of $10 * \tilde{\rho}$ (blue) and $\tilde{u}_{xtrack}$ (red) at $\lambda_{track} = 384.4$ km measured in track 1. The "PS" means "phase shift" in units of degrees, "AR" means "amplitude ratio" in units of %*s/m. (b) The same as (a) but for $\lambda_{track} = 420.7$ km measured in track 2. (c) The same as (a) but for $\lambda_{track} = 841.5$ km measured in track 3. (d) The map with GOCE data points (red dots), the location of earthquake (yellow cross) and locations of peak amplitudes measured by GOCE (green crosses). The magenta arrows denote the propagation directions and λ_H of the solved GWs. Solved intrinsic parameters and uncertainties of the GWs are shown in the magenta boxes.

Data Availability Statement

Kp, Ap and Time Series Solar Radio Flux at 10.7 cm data are available here: http://ftp.gfz-potsdam.de/pub/home/obs/Kp_ap_Ap_SN_F107/Kp_ap_Ap_SN_F107_since_1932.txt; GOCE v1.5 data and CHAMP data access is: http://thermosphere.tudelft.nl/; the Interactive Data Language (IDL) wavelet program in this paper is modified based on code used for TC98, which can be downloaded at https://github.com/ct6502/wavelets.

Acknowledgments
S. Xu and S.L. Vadas were supported by National Science Foundation (NSF) Grant AGS-1832988 and by National Aeronautics and Space Administration (NASA) Grants 80NSSC19K0836 and 80NSSC20K0628. S. Xu and J. Yue was supported by NSF Grants AGS-1651394, AGS-1834222 and by NASA Aeronomy of Ice in the Mesosphere (AIM) and 80NSSC20K0628. We thank Laboratory for Atmospheric and Space Physics (LASP) for allowing us to use the aimcips server for solving the GWs. We thank Drs. Erich Becker, Federico Gasperini, James M. Russell III, Christian Siemes, Jack Wang and Xiantong Wang for helpful discussions.

References

Aa, E., Zou, S., Eastes, R., Karan, D. K., Zhang, S. R., Erickson, P. J., & Coster, A. J. (2020). Coordinated ground-based and space-based observations of equatorial plasma bubbles. *Journal of Geophysical Research: Space Physics*, *125*(1), 1–13. https://doi.org/10.1029/2019ja027569

Alexander, M. J., Holton, J. R., & Durran, D. R. (1995). The gravity-wave response above deep convection in a squall line simulation. *Journal of the Atmospheric Sciences*, *52*(12), 2212–2226. https://doi.org/10.1175/1520-0469(1995)052<2212:tgwrad>2.0.co;2

Alexander, M. J., & Teitelbaum, H. (2007). Observation and analysis of a large amplitude mountain wave event over the Antarctic peninsula. *Journal of Geophysical Research*, *112*(D21), 1–9. https://doi.org/10.1029/2006jd008368

Alexander, M. J., & Teitelbaum, H. (2011). Three-dimensional properties of Andes mountain waves observed by satellite: A case study. *Journal of Geophysical Research*, *116*(D23), 1–10. https://doi.org/10.1029/2011jd016151

Azeem, I., Vadas, S. L., Crowley, G., & Makela, J. J. (2017). Traveling ionospheric disturbances over the United States induced by gravity waves from the 2011 Tohoku tsunami and comparison with gravity wave dissipative theory. *Journal of Geophysical Research-Space Physics*, *122*(3), 3430–3447. https://doi.org/10.1002/2016ja023659

Azeem, I., Yue, J., Hoffmann, L., Miller, S. D., Straka, W. C., & Crowley, G. (2015). Multisensor profiling of a concentric gravity wave event propagating from the troposphere to the ionosphere. *Geophysical Research Letters*, *42*(19), 7874–7880. https://doi.org/10.1002/2015gl065903

Baldwin, M. P., Gray, L. J., Dunkerton, T. J., Hamilton, K., Haynes, P. H., Randel, W. J., et al. (2001). The quasi-biennial oscillation. *Reviews of Geophysics*, *39*(2), 179–229. https://doi.org/10.1029/1999rg000073

Barth, C. A. (2010). Joule heating and nitric oxide in the thermosphere, 2. *Journal of Geophysical Research*, *115*(A10), 1–7. https://doi.org/10.1029/2010ja015565

Becker, E., Goncharenko, L., Harvey, V. L., & Vadas, S. L. (2022). Multi-step vertical coupling during the January 2017 sudden stratospheric warming. *Journal of Geophysical Research: Space Physics*, *127*(12), e2022JA030866. https://doi.org/10.1029/2022ja030866

Becker, E., & Vadas, S. L. (2020). Explicit global simulation of gravity waves in the thermosphere. *Journal of Geophysical Research: Space Physics*, *125*(10), e2020JA028034. https://doi.org/10.1029/2020ja028034

Becker, E., Vadas, S. L., Bossert, K., Harvey, V. L., Zülicke, C., & Hoffmann, L. (2022). A high-resolution whole-atmosphere model with resolved gravity waves and specified large-scale dynamics in the troposphere and stratosphere. *Journal of Geophysical Research: Atmospheres*, *127*(2), e2021JD035018. https://doi.org/10.1029/2021jd035018

Benna, M., Conde, M., England, S., Klenzing, J., Lee, Y., Qian, L., et al. (2022). The modular spectrometer for atmosphere and ionosphere characterization (MoSAIC) for the geospace dynamics constellation (GDC) mission. *Paper presented at the AGU Fall Meeting Abstracts*.

Bezděk, A. (2007). Lognormal distribution of the observed and modelled neutral thermospheric densities. *Studia Geophysica et Geodaetica*, *51*(3), 461–468. https://doi.org/10.1007/s11200-007-0027-2

Bhatt, A., Harding, B. J., Makela, J. J., Navarro, L., Lamarche, L., Valentic, T., et al. (2023). MANGO: An optical network to study the dynamics of the Earth's upper atmosphere. *Authorea Preprints*, *128*(10), 1–15. https://doi.org/10.1029/2023ja031589

Bruinsma, S. L., & Forbes, J. M. (2008). Medium-to large-scale density variability as observed by CHAMP. *Space Weather*, *6*(8), 1–9. https://doi.org/10.1029/2008sw000411

Bruinsma, S. L., & Forbes, J. M. (2009). Properties of traveling atmospheric disturbances (TADs) inferred from CHAMP accelerometer observations. *Advances in Space Research*, *43*(3), 369–376. https://doi.org/10.1016/j.asr.2008.10.031

Chen, C. (2016). *Exploration of the mystery of polar wave dynamics with lidar/radar observations and general circulation models & development of new wave analysis methods*. University of Colorado at Boulder.

Choi, H. J., Chun, H. Y., & Song, I. S. (2007). Characteristics and momentum flux spectrum of convectively forced internal gravity waves in ensemble numerical simulations. *Journal of the Atmospheric Sciences*, *64*(10), 3723–3734. https://doi.org/10.1175/jas4037.1

Cotton, W. R., & Anthes, R. A. (1992). *Storm and cloud dynamics*. Academic press.

Cowling, D., Webb, H., & Yeh, K. (1971). Group rays of internal gravity waves in a wind-stratified atmosphere. *Journal of Geophysical Research*, *76*(1), 213–220. https://doi.org/10.1029/ja076i001p00213

Crowley, G., Jones, T. B., & Dudeney, J. R. (1987). Comparison of short-period tid morphologies in Antarctica during geomagnetically quiet and active intervals. *Journal of Atmospheric and Terrestrial Physics*, *49*(11–12), 1155–1162. https://doi.org/10.1016/0021-9169(87)90098-5

Crowley, G., & Rodrigues, F. S. (2012). Characteristics of traveling ionospheric disturbances observed by the TIDDBIT sounder. *Radio Science*, *47*(4), 1–12. https://doi.org/10.1029/2011rs004959

Cullens, C. Y., England, S. L., Immel, T. J., Maute, A., Harding, B. J., Triplett, C. C., et al. (2022). Seasonal variations of medium-scale waves observed by ICON-MIGHTI. *Geophysical Research Letters*, *49*(17), 1–9. https://doi.org/10.1029/2022gl099383

Dhadly, M. S., Englert, C. R., Drob, D. P., Emmert, J. T., Niciejewski, R., & Zawdie, K. A. (2021). Comparison of ICON/MIGHTI and TIMED/TIDI neutral wind measurements in the lower thermosphere. *Journal of Geophysical Research: Space Physics*, *126*(12), e2021JA029904. https://doi.org/10.1029/2021ja029904

Doornbos, E. (2012). *Thermospheric density and wind determination from satellite dynamics*. Springer Science & Business Media.

Doornbos, E. (2019). ESA AO/1-6367/10/NL/AF "GOCE+ Theme 3: Air density and wind retrieval using GOCE data" Data Set User Manual for data set version 2.0. Dataset User Manual. https://earth.esa.int/eogateway/documents/20142/37627/GOCE-thermospheric-dataset-user-manual.pdf

Doornbos, E., Bruinsma, S., Fritsche, B., Visser, P., Van Den IJssel, J., Encarnacao, J. T., & Kern, M. (2013). Air density and wind retrieval using GOCE data. In *Paper presented at the ESA living planet symposium* (pp. 1–8).

Doornbos, E., Forster, M., Fritsche, B., van Helleputte, T., van den IJssel, J., Koppenwallner, G., et al. (2009). *ESTEC contract 21022/07/NL/HE air density models derived from multi-satellite drag observations—final report* (Vol. 1, pp. 7–39). DEOS/Delft University of Technology Scientific TR.

Doornbos, E., Van Den Ijssel, J., Luhr, H., Forster, M., & Koppenwallner, G. (2010). Neutral density and crosswind determination from arbitrarily oriented multiaxis accelerometers on satellites. *Journal of Spacecraft and Rockets*, *47*(4), 580–589. https://doi.org/10.2514/1.48114

Drob, D. P., Emmert, J. T., Meriwether, J. W., Makela, J. J., Doornbos, E., Conde, M., et al. (2015). An update to the Horizontal Wind Model (HWM): The quiet time thermosphere. *Earth and Space Science*, *2*(7), 301–319. https://doi.org/10.1002/2014ea000089

Eckermann, S. D., & Preusse, P. (1999). Global measurements of stratospheric mountain waves from space. *Science*, *286*(5444), 1534–1537. https://doi.org/10.1126/science.286.5444.1534

Emmert, J. T., Jones, M., Jr., Siskind, D. E., Drob, D. P., Picone, J. M., Stevens, M., et al. (2022). NRLMSIS 2.1: An empirical model of nitric oxide incorporated into MSIS. *Journal of Geophysical Research: Space Physics*, *127*(10), e2022JA030896. https://doi.org/10.1029/2022ja030896

Forbes, J. M., Bruinsma, S. L., Doornbos, E., & Zhang, X. L. (2016). Gravity wave-induced variability of the middle thermosphere. *Journal of Geophysical Research-Space Physics*, *121*(7), 6914–6923. https://doi.org/10.1002/2016ja022923

Fovell, R., Durran, D., & Holton, J. (1992). Numerical simulations of convectively generated stratospheric gravity waves. *Journal of the Atmospheric Sciences*, *49*(16), 1427–1442. https://doi.org/10.1175/1520-0469(1992)049<1427:nsocgs>2.0.co;2

Frissell, N. A., Baker, J. B. H., Ruohoniemi, J. M., Greenwald, R. A., Gerrard, A. J., Miller, E. S., & West, M. L. (2016). Sources and characteristics of medium-scale traveling ionospheric disturbances observed by high-frequency radars in the North American sector. *Journal of Geophysical Research: Space Physics*, *121*(4), 3722–3739. https://doi.org/10.1002/2015ja022168

Fritts, D. C. (1982). Shear excitation of atmospheric gravity-waves. *Journal of the Atmospheric Sciences*, *39*(9), 1936–1952. https://doi.org/10.1175/1520-0469(1982)039<1936:seoagw>2.0.co;2

Fritts, D. C., & Luo, Z. (1992). Gravity wave excitation by geostrophic adjustment of the jet stream. Part I: Two-dimensional forcing. *Journal of the Atmospheric Sciences*, *49*(8), 681–697. https://doi.org/10.1175/1520-0469(1992)049<0681:gwebga>2.0.co;2

Fritts, D. C., Smith, R. B., Taylor, M. J., Doyle, J. D., Eckermann, S. D., Dornbrack, A., et al. (2016). The deep propagating gravity wave experiment (DEEPWAVE): An airborne and ground-based exploration of gravity wave propagation and effects from their sources throughout the lower and middle atmosphere. *Bulletin of the American Meteorological Society*, *97*(3), 425–453. https://doi.org/10.1175/bams-d-14-00269.1

Fritts, D. C., & Vadas, S. L. (2008). Gravity wave penetration into the thermosphere: Sensitivity to solar cycle variations and mean winds. *Annales Geophysicae*, *26*(12), 3841–3861. https://doi.org/10.5194/angeo-26-3841-2008

Garcia, R. F., Bruinsma, S., Massarweh, L., & Doornbos, E. (2016). Medium-scale gravity wave activity in the thermosphere inferred from GOCE data. *Journal of Geophysical Research: Space Physics*, *121*(8), 8089–8102. https://doi.org/10.1002/2016ja022797

Garcia, R. F., Doornbos, E., Bruinsma, S., & Hebert, H. (2014). Atmospheric gravity waves due to the Tohoku-Oki tsunami observed in the thermosphere by GOCE. *Journal of Geophysical Research: Atmospheres*, *119*(8), 4498–4506. https://doi.org/10.1002/2013jd021120

Garcia, R. R., Dunkerton, T. J., Lieberman, R. S., & Vincent, R. A. (1997). Climatology of the semiannual oscillation of the tropical middle atmosphere. *Journal of Geophysical Research*, *102*(D22), 26019–26032. https://doi.org/10.1029/97jd00207

Gilman, D. L., Fuglister, F. J., & Mitchell, J. (1963). On the power spectrum of "red noise". *Journal of the Atmospheric Sciences*, *20*(2), 182–184. https://doi.org/10.1175/1520-0469(1963)020<0182:otpson>2.0.co;2

Gross, S. H., Reber, C. A., & Huang, F. T. (1984). Large-scale waves in the thermosphere observed by the Ae-C satellite. *IEEE Transactions on Geoscience and Remote Sensing*, *22*(4), 340–352. https://doi.org/10.1109/tgrs.1984.350635

Harvey, V. L., Randall, C. E., Goncharenko, L. P., Becker, E., Forbes, J. M., Carstens, J., et al. (2023). CIPS observations of gravity wave activity at the edge of the polar vortices and coupling to the ionosphere. *Journal of Geophysical Research: Atmospheres*, *128*(12), 1–23. https://doi.org/10.1029/2023jd038827

Heale, C. J., Snively, J. B., Bhatt, A. N., Hoffmann, L., Stephan, C. C., & Kendall, E. A. (2019). Multilayer observations and modeling of thunderstorm-generated gravity waves over the midwestern United States. *Geophysical Research Letters*, *46*(23), 14164–14174. https://doi.org/10.1029/2019gl085934

Hindley, N. P., Wright, C. J., Gadian, A. M., Hoffmann, L., Hughes, J. K., Jackson, D. R., et al. (2021). Stratospheric gravity waves over the mountainous island of South Georgia: Testing a high-resolution dynamical model with 3-D satellite observations and radiosondes. *Atmospheric Chemistry and Physics*, *21*(10), 7695–7722. https://doi.org/10.5194/acp-21-7695-2021

Hines, C. O. (1960). Internal atmospheric gravity waves at ionospheric heights. *Canadian Journal of Physics*, *38*(11), 1441–1481. https://doi.org/10.1139/p60-150

Hocke, K., & Schlegel, K. (1996). A review of atmospheric gravity waves and travelling ionospheric disturbances: 1982-1995. *Annales Geophysicae-Atmospheres Hydrospheres and Space Sciences*, *14*(9), 917–940. https://doi.org/10.1007/s005850050357

Hoffmann, L., Xue, X., & Alexander, M. J. (2013). A global view of stratospheric gravity wave hotspots located with Atmospheric Infrared Sounder observations. *Journal of Geophysical Research-Atmospheres*, *118*(2), 416–434. https://doi.org/10.1029/2012jd018658

Hoffmann, P., Becker, E., Singer, W., & Placke, M. (2010). Seasonal variation of mesospheric waves at northern middle and high latitudes. *Journal of Atmospheric and Solar-Terrestrial Physics*, *72*(14–15), 1068–1079. https://doi.org/10.1016/j.jastp.2010.07.002

Holt, L. A., Alexander, M. J., Coy, L., Liu, C., Molod, A., Putman, W., & Pawson, S. (2017). An evaluation of gravity waves and gravity wave sources in the Southern Hemisphere in a 7 km global climate simulation. *Quarterly Journal of the Royal Meteorological Society*, *143*(707), 2481–2495. https://doi.org/10.1002/qj.3101

Holton, J. R. (1982). The role of gravity-wave induced drag and diffusion in the momentum budget of the mesosphere. *Journal of the Atmospheric Sciences*, *39*(4), 791–799. https://doi.org/10.1175/1520-0469(1982)039<0791:trogwi>2.0.co;2

Holton, J. R., & Alexander, M. J. (1999). Gravity waves in the mesosphere generated by tropospheric convention. *Tellus Series a-Dynamic Meteorology and Oceanography*, *51*(1), 45–58. https://doi.org/10.3402/tellusb.v51i1.16259

Horinouchi, T., Nakamura, T., & Kosaka, J. i. (2002). Convectively generated mesoscale gravity waves simulated throughout the middle atmosphere. *Geophysical Research Letters*, *29*(21), 3-1. https://doi.org/10.1029/2002gl016069

Innis, J. L., & Conde, M. (2002). Characterization of acoustic-gravity waves in the upper thermosphere using dynamics Explorer 2 Wind and Temperature Spectrometer (WATS) and Neutral Atmosphere Composition Spectrometer (NACS) data. *Journal of Geophysical Research*, *107*(A12), SIA 1-1–SIA 1-22. https://doi.org/10.1029/2002ja009370

Lane, T. P., Reeder, M. J., & Clark, T. L. (2001). Numerical modeling of gravity wave generation by deep tropical convection. *Journal of the Atmospheric Sciences*, *58*(10), 1249–1274. https://doi.org/10.1175/1520-0469(2001)058<1249:nmogwg>2.0.co;2

Lane, T. P., Sharman, R. D., Clark, T. L., & Hsu, H. M. (2003). An investigation of turbulence generation mechanisms above deep convection. *Journal of the Atmospheric Sciences*, *60*(10), 1297–1321. https://doi.org/10.1175/1520-0469(2003)60<1297:aiotgm>2.0.co;2

Li, R., Lei, J., Kusche, J., Dang, T., Huang, F., Luan, X., et al. (2023). Large-scale disturbances in the upper thermosphere induced by the 2022 Tonga volcanic eruption. *Geophysical Research Letters*, *50*(3), e2022GL102265. https://doi.org/10.1029/2022gl102265

Limpert, E., Stahel, W. A., & Abbt, M. (2001). Log-normal distributions across the sciences: Keys and clues. *BioScience*, *51*(5), 341–352. https://doi.org/10.1641/0006-3568(2001)051[0341:lndats]2.0.co;2

Liu, H., Pedatella, N., & Hocke, K. (2017). Medium-scale gravity wave activity in the bottomside F region in tropical regions. *Geophysical Research Letters*, *44*(14), 7099–7105. https://doi.org/10.1002/2017gl073855

Liu, H. L., McInerney, J., Santos, S., Lauritzen, P., Taylor, M., & Pedatella, N. (2014). Gravity waves simulated by high-resolution whole atmosphere community climate model. *Geophysical Research Letters*, *41*(24), 9106–9112. https://doi.org/10.1002/2014gl062468

Liu, Y., San Liang, X., & Weisberg, R. H. (2007). Rectification of the bias in the wavelet power spectrum. *Journal of Atmospheric and Oceanic Technology*, *24*(12), 2093–2102. https://doi.org/10.1175/2007jtecho511.1

Lund, T. S., Fritts, D. C., Wan, K., Laughman, B., & Liu, H.-L. (2020). Numerical simulation of mountain waves over the southern Andes. Part I: Mountain wave and secondary wave character, evolutions, and breaking. *Journal of the Atmospheric Sciences*, *77*(12), 4337–4356. https://doi.org/10.1175/jas-d-19-0356.1

Maraun, D., & Kurths, J. (2004). Cross wavelet analysis: Significance testing and pitfalls. *Nonlinear Processes in Geophysics*, *11*(4), 505–514. https://doi.org/10.5194/npg-11-505-2004

McClintock, W. E., Eastes, R. W., Beland, S., Bryant, K. B., Burns, A. G., Correira, J., et al. (2020). Global-scale observations of the limb and disk mission implementation: 2. Observations, data pipeline, and level 1 data products. *Journal of Geophysical Research: Space Physics*, *125*(5), e2020JA027809. https://doi.org/10.1029/2020ja027809

Nicolls, M. J., Vadas, S. L., Aponte, N., & Sulzer, M. P. (2014). Horizontal parameters of daytime thermospheric gravity waves and E region neutral winds over Puerto Rico. *Journal of Geophysical Research-Space Physics*, *119*(1), 575–600. https://doi.org/10.1002/2013ja018988

Nishioka, M., Tsugawa, T., Kubota, M., & Ishii, M. (2013). Concentric waves and short-period oscillations observed in the ionosphere after the 2013 Moore EF5 tornado. *Geophysical Research Letters*, *40*(21), 5581–5586. https://doi.org/10.1002/2013gl057963

Olsen, N., Friis-Christensen, E., Floberghagen, R., Alken, P., Beggan, C. D., Chulliat, A., et al. (2013). The Swarm satellite constellation application and research facility (SCARF) and Swarm data products. *Earth Planets and Space*, *65*(11), 1189–1200. https://doi.org/10.5047/eps.2013.07.001

O'sullivan, D., & Dunkerton, T. J. (1995). Generation of inertia–gravity waves in a simulated life cycle of baroclinic instability. *Journal of the Atmospheric Sciences*, *52*(21), 3695–3716. https://doi.org/10.1175/1520-0469(1995)052<3695:goiwia>2.0.co;2

Park, J., Lühr, H., Lee, C., Kim, Y. H., Jee, G., & Kim, J. H. (2014). A climatology of medium-scale gravity wave activity in the midlatitude/low-latitude daytime upper thermosphere as observed by CHAMP. *Journal of Geophysical Research: Space Physics*, *119*(3), 2187–2196. https://doi.org/10.1002/2013ja019705

Park, J., van den Ijssel, J., & Siemes, C. (2023). Dayside upper-thermospheric density Fluctuations as observed by GRACE and GRACE-FO at ~500 km height. *Journal of Geophysical Research: Space Physics*, *128*(1), 1–15. https://doi.org/10.1029/2022ja030976

Piani, C., Durran, D., Alexander, M., & Holton, J. (2000). A numerical study of three-dimensional gravity waves triggered by deep tropical convection and their role in the dynamics of the QBO. *Journal of the Atmospheric Sciences*, *57*(22), 3689–3702. https://doi.org/10.1175/1520-0469(2000)057<3689:ansotd>2.0.co;2

Plougonven, R., Hertzog, A., & Teitelbaum, H. (2008). Observations and simulations of a large-amplitude mountain wave breaking over the Antarctic Peninsula. *Journal of Geophysical Research*, *113*(D16), 1–17. https://doi.org/10.1029/2007jd009739

Preusse, P., Dörnbrack, A., Eckermann, S. D., Riese, M., Schaeler, B., Bacmeister, J. T., et al. (2002). Space-based measurements of stratospheric mountain waves by CRISTA 1. Sensitivity, analysis method, and a case study. *Journal of Geophysical Research*, *107*(D23), CRI 6-1-CRI 6-23. https://doi.org/10.1029/2001jd000699

Richmond, A. (1978). Gravity wave generation, propagation, and dissipation in the thermosphere. *Journal of Geophysical Research*, *83*(A9), 4131–4145. https://doi.org/10.1029/ja083ia09p04131

Rodrigues, M., Foulon, B., Liorzou, F., & Touboul, P. (2003). Flight experience on CHAMP and GRACE with ultra-sensitive accelerometers and return for LISA. *Classical and Quantum Gravity*, *20*(10), S291–S300. https://doi.org/10.1088/0264-9381/20/10/332

Sánchez-Lavega, A., Lebonnois, S., Imamura, T., Read, P., & Luz, D. (2017). The atmospheric dynamics of Venus. *Space Science Reviews*, *212*(3–4), 1541–1616. https://doi.org/10.1007/s11214-017-0389-x

Sato, K., Tateno, S., Watanabe, S., & Kawatani, Y. (2012). Gravity wave characteristics in the Southern Hemisphere revealed by a high-resolution middle-atmosphere general circulation model. *Journal of the Atmospheric Sciences*, *69*(4), 1378–1396. https://doi.org/10.1175/jas-d-11-0101.1

Siemes, C., Borries, C., Bruinsma, S., Fernandez-Gomez, I., Hładczuk, N., den Ijssel, J., et al. (2023). New thermosphere neutral mass density and crosswind datasets from CHAMP, GRACE, and GRACE-FO. *Journal of Space Weather and Space Climate*, *13*, 16. https://doi.org/10.1051/swsc/2023014

Song, I.-S., Chun, H.-Y., & Lane, T. P. (2003). Generation mechanisms of convectively forced internal gravity waves and their propagation to the stratosphere. *Journal of the Atmospheric Sciences*, *60*(16), 1960–1980. https://doi.org/10.1175/1520-0469(2003)060<1960:gmocfi>2.0.co;2

Stephan, C., & Alexander, M. J. (2015). Realistic simulations of atmospheric gravity waves over the continental US using precipitation radar data. *Journal of Advances in Modeling Earth Systems*, *7*(2), 823–835. https://doi.org/10.1002/2014ms000396

Takahashi, H., Taylor, M. J., Pautet, P.-D., Medeiros, A., Gobbi, D., Wrasse, C., et al. (2009). Simultaneous observation of ionospheric plasma bubbles and mesospheric gravity waves during the SpreadFEx Campaign. In *Paper presented at the annales geophysicae* (Vol. 27, No. 4, pp. 1477–1487).

Tapley, B. D., Bettadpur, S., Watkins, M., & Reigber, C. (2004). The gravity recovery and climate experiment: Mission overview and early results. *Geophysical Research Letters*, *31*(9), 1–4. https://doi.org/10.1029/2004gl019920

Taylor, M. J., & Hapgood, M. A. (1988). Identification of a thunderstorm as a source of short period gravity waves in the upper atmospheric nightglow emissions. *Planetary and Space Science*, *36*(10), 975–985. https://doi.org/10.1016/0032-0633(88)90035-9

Torrence, C., & Compo, G. P. (1998). A practical guide to wavelet analysis. *Bulletin of the American Meteorological Society*, *79*(1), 61–78. https://doi.org/10.1175/1520-0477(1998)079<0061:apgtwa>2.0.co;2

Trinh, Q. T., Ern, M., Doornbos, E., Preusse, P., & Riese, M. (2018). Satellite observations of middle atmosphere-thermosphere vertical coupling by gravity waves. *Annales Geophysicae*, *36*(2), 425–444. https://doi.org/10.5194/angeo-36-425-2018

Vadas, S. L. (2007). Horizontal and vertical propagation and dissipation of gravity waves in the thermosphere from lower atmospheric and thermospheric sources. *Journal of Geophysical Research*, *112*(A6), 1–23. https://doi.org/10.1029/2006ja011845

Vadas, S. L., & Becker, E. (2019). Numerical modeling of the generation of tertiary gravity waves in the mesosphere and thermosphere during strong mountain wave events over the southern Andes. *Journal of Geophysical Research-Space Physics*, *124*(9), 7687–7718. https://doi.org/10.1029/2019ja026694

Vadas, S. L., Becker, E., Bossert, K., Baumgarten, G., Hoffmann, L., & Harvey, V. L. (2023). Secondary gravity waves from the stratospheric polar vortex over ALOMAR observatory on 12–14 January 2016: Observations and modeling. *Journal of Geophysical Research: Atmospheres*, *128*(2), e2022JD036985. https://doi.org/10.1029/2022jd036985

Vadas, S. L., Becker, E., Figueiredo, C., Bossert, K., Harding, B. J., & Gasque, L. C. (2023). Primary and secondary gravity waves and large-scale wind changes generated by the Tonga volcanic eruption on 15 January 2022: Modeling and comparison with ICON-MIGHTI winds. *Journal of Geophysical Research: Space Physics*, *128*(2), e2022JA031138. https://doi.org/10.1029/2022ja031138

Vadas, S. L., & Crowley, G. (2010). Sources of the traveling ionospheric disturbances observed by the ionospheric TIDDBIT sounder near Wallops Island on 30 October 2007. *Journal of Geophysical Research*, *115*(A7), 1–24. https://doi.org/10.1029/2009ja015053

Vadas, S. L., Figueiredo, C., Becker, E., Huba, J., Themens, D. R., Hindley, N. P., et al. (2023). Traveling ionospheric disturbances induced by the secondary gravity waves from the Tonga eruption on 15 January 2022: Modeling with MESORAC-HIAMCM-SAMI3 and comparison with GPS/TEC and ionosonde data. *Journal of Geophysical Research: Space Physics*, *128*(6), e2023JA031408. https://doi.org/10.1029/2023ja031408

Vadas, S. L., & Fritts, D. C. (2005). Thermospheric responses to gravity waves: Influences of increasing viscosity and thermal diffusivity. *Journal of Geophysical Research*, *110*(D15), 1–16. https://doi.org/10.1029/2004jd005574

Vadas, S. L., Fritts, D. C., & Alexander, M. J. (2003). Mechanism for the generation of secondary waves in wave breaking regions. *Journal of the Atmospheric Sciences*, *60*(1), 194–214. https://doi.org/10.1175/1520-0469(2003)060<0194:mftgos>2.0.co;2

Vadas, S. L., & Liu, H. L. (2009). Generation of large-scale gravity waves and neutral winds in the thermosphere from the dissipation of convectively generated gravity waves. *Journal of Geophysical Research*, *114*(A10), 1–25. https://doi.org/10.1029/2009ja014108

Vadas, S. L., & Liu, H. L. (2013). Numerical modeling of the large-scale neutral and plasma responses to the body forces created by the dissipation of gravity waves from 6 h of deep convection in Brazil. *Journal of Geophysical Research-Space Physics*, *118*(5), 2593–2617. https://doi.org/10.1002/jgra.50249

Vadas, S. L., Liu, H. L., & Lieberman, R. S. (2014). Numerical modeling of the global changes to the thermosphere and ionosphere from the dissipation of gravity waves from deep convection. *Journal of Geophysical Research-Space Physics*, *119*(9), 7762–7793. https://doi.org/10.1002/2014ja020280

Vadas, S. L., Makela, J. J., Nicolls, M. J., & Milliff, R. F. (2015). Excitation of gravity waves by ocean surface wave packets: Upward propagation and reconstruction of the thermospheric gravity wave field. *Journal of Geophysical Research-Space Physics*, *120*(11), 9748–9780. https://doi.org/10.1002/2015ja021430

Vadas, S. L., & Nicolls, M. J. (2012). The phases and amplitudes of gravity waves propagating and dissipating in the thermosphere: Theory. *Journal of Geophysical Research*, *117*(A5), 1–25. https://doi.org/10.1029/2011ja017426

Vadas, S. L., Xu, S., Yue, J., Bossert, K., Becker, E., & Baumgarten, G. (2019). Characteristics of the quiet-time hot spot gravity waves observed by GOCE over the southern Andes on 5 July 2010. *Journal of Geophysical Research: Space Physics*, *124*(8), 7034–7061. https://doi.org/10.1029/2019ja026693

Vadas, S. L., Zhao, J., Chu, X. Z., & Becker, E. (2018). The excitation of secondary gravity waves from local body forces: Theory and observation. *Journal of Geophysical Research-Atmospheres*, *123*(17), 9296–9325. https://doi.org/10.1029/2017jd027970

Visser, T., Doornbos, E. N., de Visser, C. C., Visser, P. N., & Fritsche, B. (2018). Torque model verification for the GOCE satellite. *Advances in Space Research*, *62*(5), 1114–1136. https://doi.org/10.1016/j.asr.2018.06.025

Waldock, J., & Jones, T. (1984). The effects of neutral winds on the propagation of medium-scale atmospheric gravity waves at mid-latitudes. *Journal of Atmospheric and Terrestrial Physics*, *46*(3), 217–231. https://doi.org/10.1016/0021-9169(84)90149-1

Waldock, J., & Jones, T. (1986). HF Doppler observations of medium-scale travelling ionospheric disturbances at mid-latitudes. *Journal of Atmospheric and Terrestrial Physics*, *48*(3), 245–260. https://doi.org/10.1016/0021-9169(86)90099-1

Watanabe, S., Kawatani, Y., Tomikawa, Y., Miyazaki, K., Takahashi, M., & Sato, K. (2008). General aspects of a T213L256 middle atmosphere general circulation model. *Journal of Geophysical Research*, *113*(D12), 1–23. https://doi.org/10.1029/2008jd010026

Wright, C. J., Hindley, N. P., Alexander, M. J., Barlow, M., Hoffmann, L., Mitchell, C. N., et al. (2022). Surface-to-space atmospheric waves from Hunga Tonga-Hunga Ha'apai eruption. *Nature*, *609*(7928), 741–746. https://doi.org/10.1038/s41586-022-05012-5

Wu, D. L., & Zhang, F. Q. (2004). A study of mesoscale gravity waves over the North Atlantic with satellite observations and a mesoscale model. *Journal of Geophysical Research*, *109*(D22), 1–14. https://doi.org/10.1029/2004jd005090

Wüst, S., & Bittner, M. (2006). Non-linear resonant wave–wave interaction (triad): Case studies based on rocket data and first application to satellite data. *Journal of Atmospheric and Solar-Terrestrial Physics*, *68*(9), 959–976. https://doi.org/10.1016/j.jastp.2005.11.011

Xu, S., Carstens, J. N., France, J., Randall, C., Yue, J., Harvey, V. L., et al. (2023). Seasonal distribution of gravity waves near the stratopause in 2019–2022. *Earth and Space Science*, *10*, e2023EA003076. https://doi.org/10.1029/2023EA003076

Xu, S., Vadas, S. L., & Yue, J. (2021). Thermospheric traveling atmospheric disturbances in austral winter from GOCE and CHAMP. *Journal of Geophysical Research: Space Physics*, *126*(9), 1–22. https://doi.org/10.1029/2021ja029335

Xu, S., Yue, J., Xue, X., Vadas, S. L., Miller, S. D., Azeem, I., et al. (2019). Dynamical coupling between Hurricane Matthew and the middle to upper atmosphere via gravity waves. *Journal of Geophysical Research: Space Physics*, *124*(5), 3589–3608. https://doi.org/10.1029/2018ja026453

Yee, J.-H., Talaat, E. R., Christensen, A. B., Killeen, T. L., Russell, J. M., & Woods, T. N. (2003). TIMED instruments. *Johns Hopkins APL Technical Digest*, *24*(2), 156–164.

Yoshiki, M., & Sato, K. (2000). A statistical study of gravity waves in the polar regions based on operational radiosonde data. *Journal of Geophysical Research*, *105*(D14), 17995–18011. https://doi.org/10.1029/2000jd900204

Yue, J., Miller, S. D., Straka, W., Noh, Y. J., Chou, M. Y., Kahn, R., & Flower, V. (2022). La Soufriere volcanic eruptions launched gravity waves into space. *Geophysical Research Letters*, *49*(8), e2022GL097952. https://doi.org/10.1029/2022gl097952

Yue, J., Vadas, S. L., She, C.-Y., Nakamura, T., Reising, S. C., Liu, H.-L., et al. (2009). Concentric gravity waves in the mesosphere generated by deep convective plumes in the lower atmosphere near Fort Collins, Colorado. *Journal of Geophysical Research*, *114*(D6), 1–12. https://doi.org/10.1029/2008jd011244

Zhang, F. (2004). Generation of mesoscale gravity waves in upper-tropospheric jet–front systems. *Journal of the Atmospheric Sciences*, *61*(4), 440–457. https://doi.org/10.1175/1520-0469(2004)061<0440:gomgwi>2.0.co;2